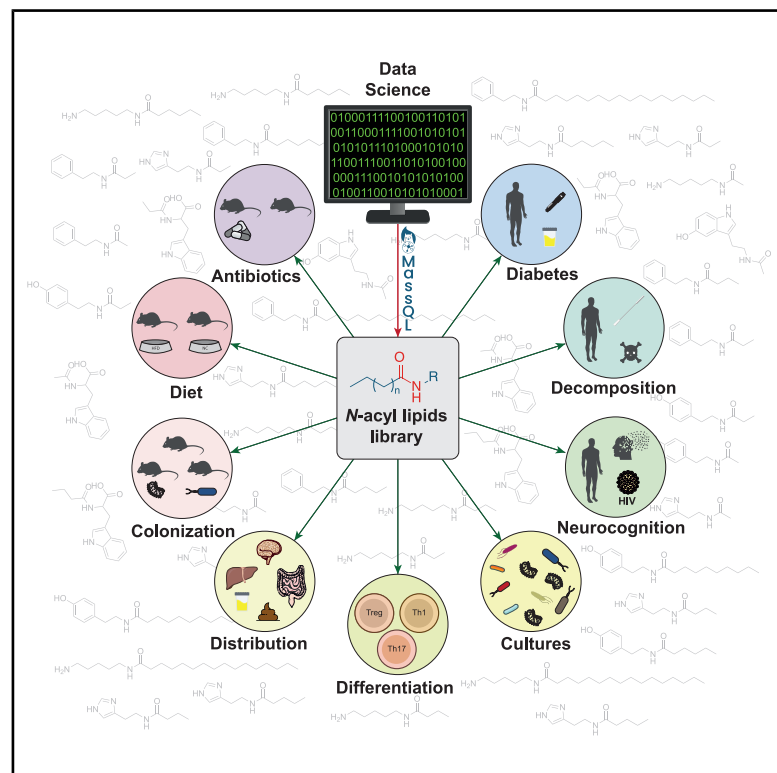


The microbiome diversifies long- to short-chain fatty acid-derived *N*-acyl lipids

Graphical abstract



Authors

Helena Mannocho-Russo,
Vincent Charron-Lamoureux,
Martijn van Faassen, ..., Dionicio Siegel,
Rob Knight, Pieter C. Dorrestein

Correspondence

pdorrestein@health.ucsd.edu

In brief

Mass spectrometry data mining tools enabled the creation of an MS/MS spectral library containing hundreds of *N*-acyl lipids, including conjugates with short-chain fatty acids. This resource enabled the discovery of associations between microbially derived *N*-acyl lipids and several phenotypes, including HIV status and cognitive impairment.

Highlights

- MS/MS data mining enables the creation of an *N*-acyl lipid spectral library resource
- Short-chain fatty acid-derived *N*-acyl lipids are described
- *N*-acyl histamines and cadaverines are linked to HIV and neurocognitive impairment
- *N*-acyl cadaverines show immunomodulatory effects of T cells



Resource

The microbiome diversifies long- to short-chain fatty acid-derived *N*-acyl lipids

Helena Mannocho-Russo,¹ Vincent Charron-Lamoureux,¹ Martijn van Faassen,^{1,2} Santosh Lamichhane,^{1,3} Wilhan D. Gonçalves Nunes,¹ Victoria Deleray,¹ Adriana V. Ayala,⁴ Yuichiro Tanaka,⁴ Abubaker Patan,¹ Kyle Vittali,¹ Prajit Rajkumar,¹ Yasin El Abiead,¹ Haoqi Nina Zhao,¹ Paulo Wender Portal Gomes,¹ Ipsita Mohanty,¹ Carlynda Lee,¹ Aidan Sund,¹ Meera Sharma,¹ Yuanhao Liu,¹ David Pattynama,¹ Gregory T. Walker,⁵ Grant J. Norton,⁵ Lora Khatib,^{6,7} Mohammadsobhan S. Andalibi,^{6,8,9,10} Crystal X. Wang,^{9,10} Ronald J. Ellis,^{8,10}

(Author list continued on next page)

¹Skaggs School of Pharmacy and Pharmaceutical Sciences, University of California, San Diego, La Jolla, CA 92093, USA

²Department of Laboratory Medicine, University of Groningen, University Medical Center Groningen, 9713 GZ Groningen, the Netherlands

³Institute of Biomedicine, Faculty of Medicine, University of Turku & Turku Bioscience Center, University of Turku and Åbo Akademi University, 20520 Turku, Finland

⁴Department of Pathology, University of California, San Diego, La Jolla, CA 92093, USA

⁵Division of Host-Microbe Systems & Therapeutics, Department of Pediatrics, University of California, San Diego, La Jolla, CA 92093, USA

⁶Department of Pediatrics, University of California, San Diego, La Jolla, CA 92093, USA

⁷Neurosciences Graduate Program, University of California, San Diego, La Jolla, CA 92093, USA

⁸Department of Neurosciences, University of California, San Diego, La Jolla, CA 92093, USA

⁹Department of Psychiatry, University of California, San Diego, La Jolla, CA 92093, USA

¹⁰HIV Neurobehavioral Research Program, University of California, San Diego, La Jolla, CA 92093, USA

¹¹Department of Medicine, University of California, San Diego, La Jolla, CA 92093, USA

¹²Department of Bioengineering, University of California, San Diego, La Jolla, CA 92093, USA

¹³Center for Microbiome Innovation, University of California, San Diego, La Jolla, CA 92093, USA

¹⁴Larsson-Rosenquist Foundation Mother-Milk-Infant Center of Research Excellence (MOMI CORE) and the Human Milk Institute (HMI), University of California, San Diego, La Jolla, CA 92093, USA

¹⁵Department of Immunology, Harvard Medical School, Boston, MA 02115, USA

¹⁶Key Laboratory of Multi-Cell Systems, Shanghai Institute of Biochemistry and Cell Biology, Center for Excellence in Molecular Cell Science, Chinese Academy of Sciences, University of Chinese Academy of Sciences, Shanghai 200031, China

¹⁷Department of Microbiology, University of Tennessee, Knoxville, TN 37996, USA

¹⁸Department of Pediatrics, Division of Pediatric Endocrinology, University of California, San Diego, La Jolla, CA 92093, USA

¹⁹Rady Children's Hospital San Diego, San Diego, CA 92123, USA

²⁰Division of Pediatric Endocrinology, Children's Hospital of Orange County, Orange, CA 92868, USA

(Affiliations continued on next page)

SUMMARY

N-Acyl lipids are important mediators of several biological processes including immune function and stress response. To enhance the detection of *N*-acyl lipids with untargeted mass spectrometry-based metabolomics, we created a reference spectral library retrieving *N*-acyl lipid patterns from 2,700 public datasets, identifying 851 *N*-acyl lipids that were detected 356,542 times. 777 are not documented in lipid structural databases, with 18% of these derived from short-chain fatty acids and found in the digestive tract and other organs. Their levels varied with diet and microbial colonization and in people living with diabetes. We used the library to link microbial *N*-acyl lipids, including histamine and polyamine conjugates, to HIV status and cognitive impairment. This resource will enhance the annotation of these compounds in future studies to further the understanding of their roles in health and disease and to highlight the value of large-scale untargeted metabolomics data for metabolite discovery.

INTRODUCTION

N-Acyl lipids are signaling molecules consisting of two components: a fatty acid and an amine group, linked by an amide bond (Figure 1A). The previously described *N*-acyl lipids are involved in crucial biological functions, including immune ho-

meostasis, building of fat mass levels, and regulation of energy expenditure related to obesity, and they regulate other processes such as pain, memory, and insulin levels.^{1–6} Representative examples include *N*-oleoylethanolamine, which controls food intake; *N*-acyl taurine, which improves insulin sensitivity; and *N*-arachidonoyl 3-OH- γ -aminobutyric acid, which regulates



David J. Moore,^{9,10} Jennifer E. Iudicello,^{9,10} Donald Franklin Jr.,^{9,10} Scott Letendre,^{10,11} Loryn Chin,^{6,12,13} Corinn Walker,⁶ Simone Renwick,^{6,14} Jasmine Zemlin,^{1,13} Michael J. Meehan,¹ Xinyang Song,^{15,16} Dennis Kasper,¹⁵ Zachary Burcham,¹⁷ Jane J. Kim,^{18,19} Sejal Kadakia,²⁰ Manuela Raffatellu,^{5,13,21} Lars Bode,^{6,14} Hiutung Chu,^{4,13,21} Karsten Zengler,^{6,12,13} Mingxun Wang,²² Dionicio Siegel,¹ Rob Knight,^{6,13,23,24,25} and Pieter C. Dorrestein^{1,13,26,27,28,*}

²¹Chiba University - UC San Diego Center for Mucosal Immunology, Allergy, and Vaccines, La Jolla, CA 92093, USA

²²Department of Computer Science and Engineering, University of California, Riverside, Riverside, CA 92521, USA

²³Department of Computer Science and Engineering, University of California, San Diego, La Jolla, CA 92093, USA

²⁴Halicioğlu Data Science Institute, University of California, San Diego, La Jolla, CA 92093, USA

²⁵Shu Chien-Gene Lay Department of Bioengineering, University of California, San Diego, La Jolla, CA 92093, USA

²⁶Collaborative Mass Spectrometry Innovation Center, Skaggs School of Pharmacy and Pharmaceutical Sciences, University of California, San Diego, La Jolla, CA 92093, USA

²⁷Department of Pharmacology, University of California, San Diego, La Jolla, CA 92093, USA

²⁸Lead contact

*Correspondence: pdorrestein@health.ucsd.edu

<https://doi.org/10.1016/j.cell.2025.05.015>

calcium-dependent voltage channel function.^{7,8} Other *N*-acyl lipids, such as *N*-acetyl cysteine and *N*^α-lauroyl-L-arginate, are used as an FDA-approved drug and a food ingredient, respectively. *N*-Acetyl cysteine has antioxidant and anti-inflammatory properties and is used to block acetaminophen poisoning, as well as to break up mucus in respiratory diseases.⁹ On the other hand, *N*^α-lauroyl-L-arginate acts as an antimicrobial agent, inhibiting bacteria, yeasts, and molds in food products.⁸ These are only a few examples of *N*-acyl lipids, but these molecules are chemically very diverse. LIPID MAPS, one of the most comprehensive lipid structural databases,¹⁰ currently catalogs close to 400 *N*-acyl lipids comprising 76 different head groups derived from primary amines or amino acids (Figures S1A and S1B).

Known *N*-acyl lipids can be identified through targeted mass spectrometry (MS) approaches,^{11–14} but both known and previously unreported *N*-acyl lipids often go unannotated in untargeted metabolomics data owing to the lack of reference MS/MS spectra. We hypothesized that many *N*-acyl lipids relevant to biology exist within publicly available liquid chromatography-tandem mass spectrometry (LC-MS/MS) untargeted metabolomics data but remain unannotated because of the absence of relevant spectral libraries. Building on these efforts, we developed a strategy to create a reusable *N*-acyl lipid resource to reinterpret existing data from the untargeted metabolomics repository, GNPS/MassIVE. In this way, the biological function of *N*-acyl lipids in different contexts can be elucidated, and we can ensure that future untargeted metabolomics studies will not overlook these important metabolites. Our approach leverages the reverse metabolomics strategy,¹⁵ where MS/MS spectra can serve as proxies for metabolites, which are then matched across public studies to contextualize their biological relevance.^{14,16–23}

RESULTS

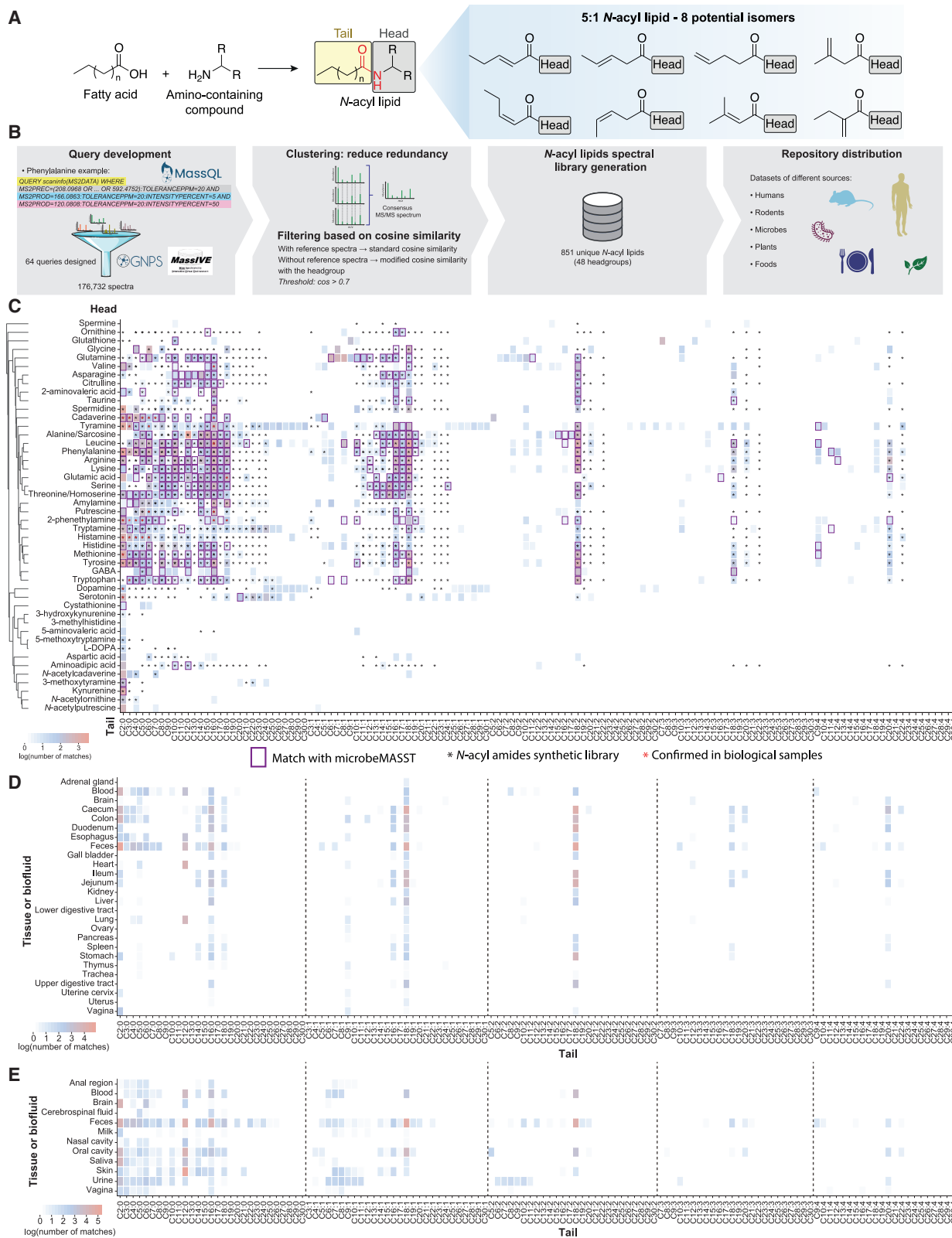
Detection of *N*-acyl lipids in public data

To uncover the presence of *N*-acyl lipids and improve their detection in existing public untargeted metabolomics data, we developed the Mass Spec Query Language (MassQL) queries²¹ for 8,256 different *N*-acyl lipids with 64 amines and amino acids as head groups (Figures 1B, S1C, and S1D; Table S1). We applied these queries to filter MS/MS data from the GNPS-based untargeted metabolomics data (2,706 datasets as of January 2024

and includes ~1.2 billion MS/MS spectra). The fragmentation-based queries were confined to 2- to 30-carbon fatty acids with up to four unsaturations. This range was selected because these fatty acids fragment predictably because of the limited presence of internal fragments, making it more straightforward to develop specific queries for which we could keep low false discovery rates (FDRs) (STAR Methods; Figures S1C and S1D). Of the 64 head groups for which we created queries, 41 have not been documented in comprehensive curated lipid structure databases such as LIPID MAPS,¹⁰ LipidBANK,²⁴ or SwissLipids,²⁵ making their existence and/or prevalence in biology, including human biology, unclear (Figures S1A and S1B).²⁶

Of the 64 amines and amino acid head groups, we found that 46 were linked with 2- to 30-carbon fatty acids in public data (Figure 1C). These represented 851 compounds of the theoretically 8,256 possible candidates from our initial MassQL searches (Figure 1C; Table S1). A reusable MS/MS spectral library was created as a resource to enable other researchers to investigate *N*-acyl lipids in MS-based metabolomics studies in the future (Figure 1B). We found that this spectral library can also potentially serve as a valuable resource for lipidomics research, as *N*-acyl lipids were also successfully annotated in multiple datasets where extraction conditions commonly used in lipidomics studies were applied (Table S1). 552 spectra were confirmed to match their MS/MS using reference MS/MS of standards created using combinatorial organic synthesis^{14,27} (Figure 1C). These represent level 2 or 3 annotations according to both the 2007 Metabolomics Standards Initiative and the 2014 Schymanski rules for untargeted metabolomics annotation.^{28,29} In the absence of physical samples, this is the highest level of annotation currently possible for annotating MS/MS data in public data.

The most frequently detected lipid conjugate was acetylation (C2).²⁶ While saturated carbons were the most common, an unexpected finding was the prevalence of both saturated and unsaturated C3–C6 short-chain fatty acid (SCFA)-derived *N*-acyl lipids, which are rarely reported in the lipid structural databases (Figure S1B).^{10,25,26} Irrespective of fatty acid length, the saturated fatty acid containing *N*-acyl lipids were detected most frequently—followed by one, two, three, and four unsaturations. The most common fatty acids linked to *N*-acyl lipids were C18:1 and C16:1 for one double bond and C18:2, C18:3, and C20:4 for two, three, and four unsaturations, respectively. Very long-chain-linked *N*-acyl lipids are less frequently observed. Even-carbon



(legend on next page)

lipid chains accounted for 87% of matches (Table S1). Tyramine had the highest number of different fatty acid attachments, followed by leucine, phenylalanine, and tryptamine. Glutamine was associated with rare C8–C18 lipids, while tyramine, tryptamine, dopamine, and serotonin had rare C20–C30 lipid attachments (Figure 1C).

With the *N*-acyl lipid MS/MS spectra obtained using MassQL,²¹ we performed a MASST^{19,30} search against the entire GNPS repository to link the retrieved spectra to their biological associations. We obtained 356,542 MS/MS spectra from 61,833 files across 950 datasets, highlighting the widespread detection of *N*-acyl lipids in untargeted metabolomics studies. As little is known about the biology associated with *N*-acyl lipids, we leveraged the reverse metabolomics strategy¹⁴ to understand their presence in rodents and humans and their distribution across organs, biofluids, and other sources such as food, plants, or microbial cultures. By considering additional metadata curated with controlled vocabularies using the ReDU²⁰ infrastructure in GNPS,²² we could categorize *N*-acyl lipids detected in tissues and biofluids from humans and rodents, representing 435 and 259 *N*-acyl lipids, respectively. The tissue and biofluid distribution in rodents and humans, including the number of MS/MS spectra, unique *N*-acyl lipids head groups, and different acyl chain lengths, are depicted in Figures S2A and S2B. We observed an overlap of 205 *N*-acyl lipids in public data from both human and rodent-related datasets, with fecal samples contributing the most to this overlap (Figure S2C). The most frequently observed chain lengths in both humans and rodents were C2, C12, C16, and C18, as illustrated in Figures 1D and 1E. Odd-chain lipid chains were also detected in both human and rodent datasets, with C3:0 (propionate) and C5:0 (valerate), both classified as short-chain fatty acid-derived molecules, being the most frequently detected among them. In rodents, C3:0 was primarily observed in the colon, caecum, esophagus, and feces, while C5:0 was mostly found in feces and blood. In humans, C3:0 was detected in saliva, the vagina, and feces, while C5:0 was present in the oral cavity, urine, blood, and cerebrospinal fluid, in addition to feces. The most common head groups identified in both humans and rodents were phenylalanine, spermidine, (iso)leucine, and alanine/sarcosine (Figures S2D and S2E). The data suggests that *N*-acyl lipids occupy specific body niches. Aspartic acid, amino adipic acid, and spermidine lipids were primarily found in the brain and rarely in other body locations. Spermidine-conjugated lipids appeared frequently in saliva, while glutamine *N*-acyl lipids were more common in blood, skin, and urine. Tyrosine-conjugated lipids, however, were almost exclusively detected in human milk.

Out of the 851 *N*-acyl lipids, 347 were detected in data from microbial cultures using microbeMASST¹⁶ (Figures 1C, 2A, and 2B; Table S1), which consist of a curated reference database of LC-MS/MS data from more than 60,000 microbial monocultures, comprising 1,858 unique taxonomic lineages. The most commonly observed *N*-acyl lipids in these microbial monocultures had phenylalanine, leucine, and tyrosine as head groups (Figure 2A), with an overall predominance of even-chain lengths (Figure 2B). Additionally, 167 and 243 of the 851 candidate *N*-acyl lipids were detected in plant and food datasets, respectively (Figure 2C; Table S2). This distribution stratified by lipid chain length revealed that short-, medium-, and long-chain conjugates are predominantly detected in human, microbial, and rodent-related datasets, while very long-chain *N*-acyl lipids are observed almost exclusively in plants and foods (Figures 2D and S3A–S3D). It is important to note that extraction protocols and chromatographic conditions used in the datasets deposited in the public domain could impact these observations. However, we investigated these variables in the spectra retrieved in our analyses, and they are largely comparable across different sources (Figure S3E; Table S2). Both lipidomics and metabolomics datasets were retrieved, highlighting their relevance at the intersection of both omics. These differences in *N*-acyl lipids found in food and plant data, compared with microbial cultures, rodent, and human datasets, suggest they may be consumed through diet but may also be produced by the microbiota.

This hypothesis was further evaluated by the analysis of a public dataset of small intestine and colon samples, where germ-free (GF) mice were colonized with a conventional gut microbiota (specific pathogen-free, SPF) or monocolonized with segmented filamentous bacteria (SFB) or other gut commensal strains.^{32,33} In addition, we conducted another culturing experiment with human-derived microbiota to enable MS/MS and retention time matching. Both datasets revealed a mixture of both consumption and production of *N*-acyl lipids, providing additional evidence that the microbiota regulates *N*-acyl lipid levels. These results are also consistent with a recent report of a *Faecalibacterium prausnitzii* hydrolase that has both amide hydrolase and *N*-acylation function.³⁴

The *N*-acyl lipid profile in the small intestine and colon differed in mice colonized with conventional microbiota (SPF) or monocolonized with SFB, compared with GF mice. In addition, the reanalysis of other monocolonized mouse samples revealed that short-chain fatty acids generally increased, while those conjugated with longer chains decreased, compared with GF mice, with cases of microbe specificity, supporting the hypothesis that microbes may be

Figure 1. Repository-scale analysis of *N*-acyl lipids in public mass spectrometry data and distribution among different tissues or biofluids

(A) *N*-Acyl lipid definitions and isomers: this panel explains *N*-acyl lipids using a C5:1 tail example. A C5:1 lipid consists of a five-carbon fatty acid with one double bond. The image illustrates the possible isomers for this structure that can yield the same MS/MS spectrum.

(B) Summary of the workflow followed to generate the *N*-acyl lipids spectral library and repository-scale searches. More detailed information on each step is available in Figures S1C–S1E.

(C) Heatmap of *N*-acyl lipids: the heatmap shows 851 *N*-acyl lipids identified from public MS data in the MassIVE/GNPS repository using MassQL queries.²¹ Compounds found in microbial cultures are marked with purple squares, those matched with synthetic standards are indicated by black stars, and those confirmed by retention time with biological samples are shown with red stars.

(D and E) Heatmaps showing distribution in tissues and biofluids: number of matches of different fatty acid chain lengths in tissues and biofluids with metadata available in ReDU²⁰ for (D) rodent and (E) human-related public datasets. All heatmaps are shown as log values of the matches obtained from the repository, regardless of the head group. Icons were obtained from Bioicons.com.

Related to Figures S1 and S2.

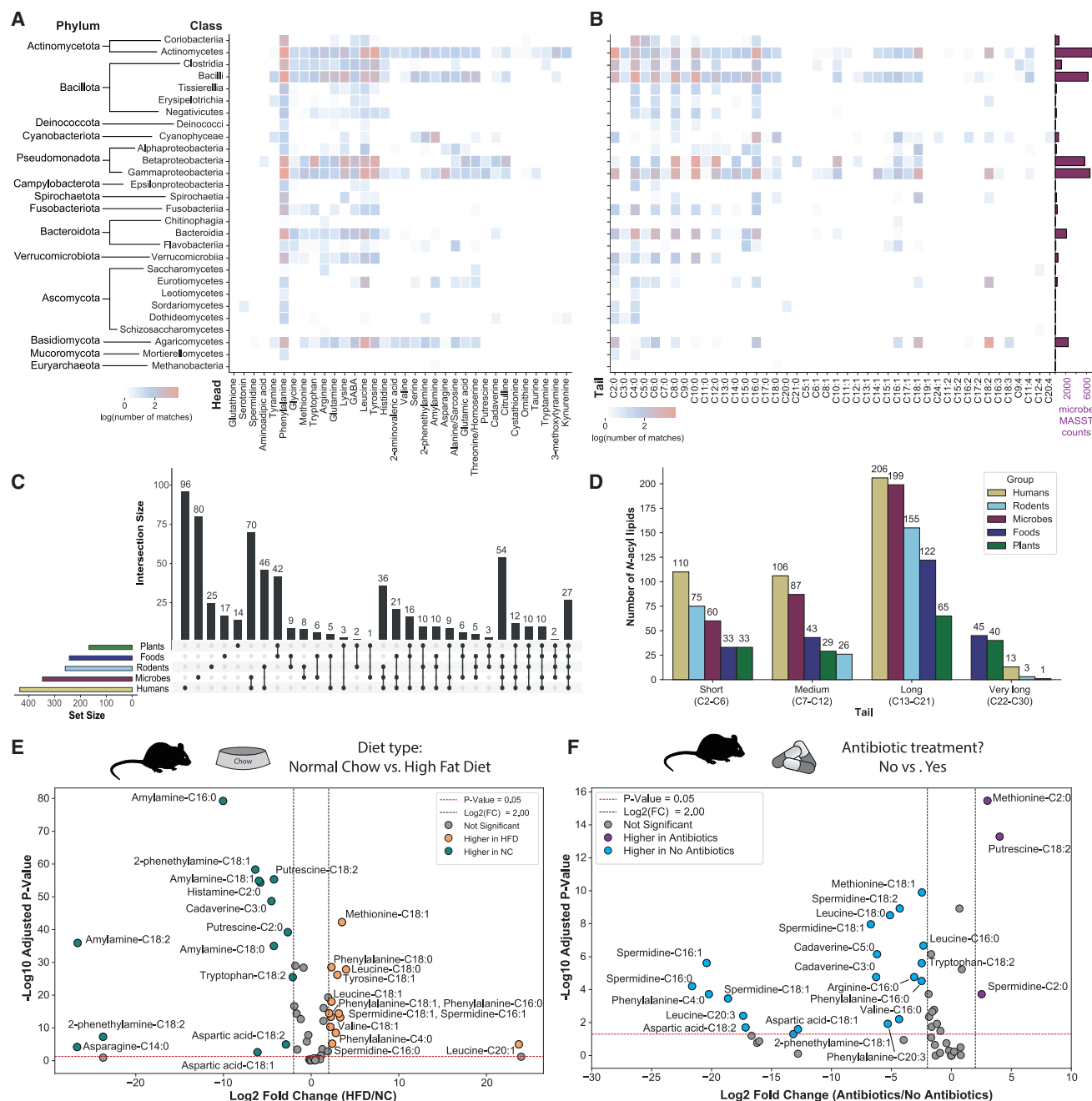


Figure 2. Evidence of microbial origins of *N*-acyl lipids

(A and B) Heatmaps depict the distribution of different head groups (A) and tails (B) across various microbial classes, with barplots showing the total counts for each class in microbeMASST.¹⁶ The y axis was taxonomically ordered according to the NCBI Taxonomy ID, while the x axis was clustered using the BrayCurtis metric for the head groups or in ascending order (in number of carbons and unsaturations) for the tails.

(C) UpSet plot of *N*-acyl lipid distribution: this plot highlights the distribution of *N*-acyl lipids across different datasets, including human-related, rodent-related, microbial monocultures, and plant- and food-associated data.

(D) Distribution of *N*-acyl lipid chain lengths: this summary shows the prevalence of short-, medium-, long-, and very long-chain *N*-acyl lipids in public data. Note that the exact location and *cis/trans* configurations of double bonds cannot be determined from the current queries, which are annotated at the molecular family level according to the Metabolomics Standards Initiative.²⁸

(legend continued on next page)

involved in *N*-acyl lipids production (Figure S3F). Culturing 71 commensal bacteria from the human gut also revealed their ability to make *N*-acyl lipids and provided additional support for this hypothesis.³⁵ Since the vast majority of these microbes are not yet part of microbeMASST, this approach provided both orthogonal evidence and experimental validation of microbial-linked *N*-acyl lipids. We obtained 50 MS/MS matches to the *N*-acyl lipids resource, with 38 corresponding to *N*-acyl lipids conjugated to short-chain fatty acids (Figures S3G, S4A, and S4B). We observed that short-chain *N*-acyl lipids increased, compared with the culture media, while longer chains (C8–C12) generally decreased, except for ornithine-C17:1 and leucine- and methionine-C9:4, suggesting that the microbiota can produce many of these *N*-acyl lipids conjugated to short-chain fatty acids.

To assess the presence of *N*-acyl lipids and their potential changes under different biological conditions, we performed in-depth analyses using our newly created library on public datasets that had expanded metadata. Reanalysis of datasets on diabetes (type I), various stages of forensic human body decompositions,³⁶ and diet and effect of antibiotics in colorectal cancer³¹ revealed the presence of many *N*-acyl lipids, based on matching their MS/MS against the MS/MS *N*-acyl lipids resource (Figures 2E, 2F, and S3H–S3N). Peak intensity analysis against the available metadata revealed that shorter-chain *N*-acyl lipids were decreased in the diabetic group (urine from humans) (Figure S3H), longer-chain fatty acids *N*-acyl lipids increased upon cadaver decomposition (skin swabs from humans and soil) (Figures S3I–S3L, S4D, and S4E), and overall *N*-acyl lipids levels were altered by diet (feces of mice on normal chow vs. high-fat diet) (Figure 2E). Mice on a normal chow had a higher abundance and variety of short-chain fatty acid-derived *N*-acyl lipids, compared with mice on a high-fat diet. Conversely, mice on a high-fat diet showed increases in *N*-acyl lipids conjugated to longer-chain fatty acids (Figures 2E and S3M). Intriguingly, most of those same longer-chain fatty acid conjugates that are observed in the high-fat diet are no longer detected upon treatment with an antibiotic cocktail (Figures 2F and S3N), providing additional evidence linking the production of many of the *N*-acyl lipids conjugates to the microbiome and diet. After generating and validating the *N*-acyl lipid resource with published datasets and with the knowledge that many *N*-acyl lipids are made by the microbiota, we next set out to demonstrate its utility in a new human research study.

Demonstrating the utility of the *N*-acyl lipid resource—*N*-acyl lipids in relation to HIV, immune, and cognition status

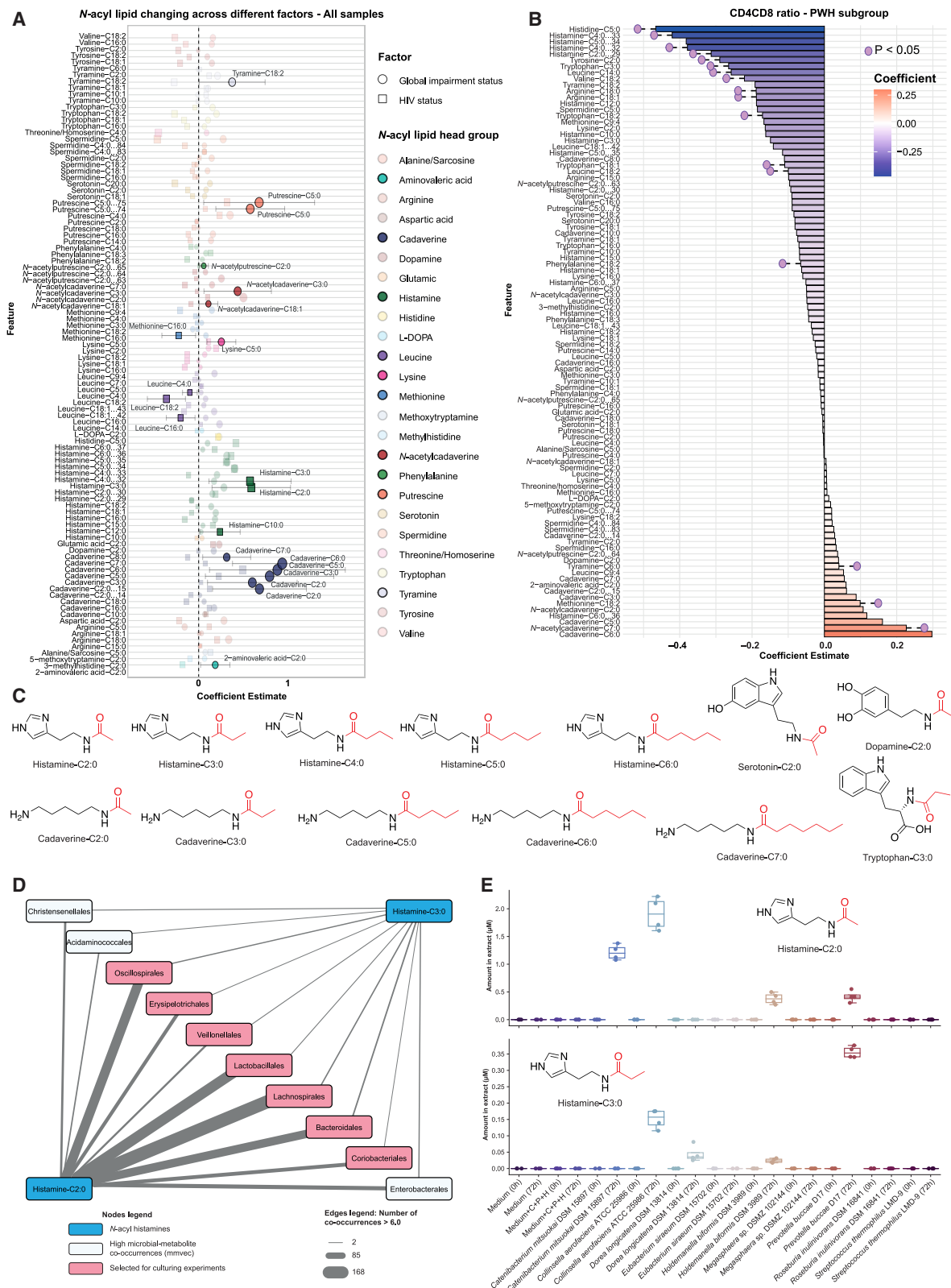
To further demonstrate the utility of our newly created *N*-acyl lipid MS/MS library, and to provide a case study on how to leverage this resource, we used it to annotate *N*-acyl lipids in an ongoing study in our laboratory aimed at understanding the effect of the microbiome on neurocognition in people infected with the human immunodeficiency virus (HIV). This cohort

included stool data collected from both people with HIV (PWH) and people without HIV (PWoH), who had also completed neurocognitive evaluations as part of NIH-funded studies conducted at the UC San Diego HIV Neurobehavioral Research Program, primarily the HIV Neurobehavioral Research Center (HNRC). The characteristics of the participants are available in Table S3. More than 50 matches to MS/MS spectra of *N*-acyl lipids were obtained, and we observed higher levels of histamine *N*-acyl lipids, particularly those conjugated with short-chain fatty acids, in PWH compared with PWoH (Figure S5A). In pairwise comparisons of specific *N*-acyl lipids, histamine-C2:0, histamine-C3:0, and histamine-C6:0 were higher in PWH (Mann-Whitney U test, *p* values of 0.003, 0.003, and 0.042, respectively). Besides that, histamine-C4:0 and histamine-C5:0 also showed a higher trend in PWH. All other *N*-acyl histamines, including those not initially searched for with the MassQL query but identified through molecular networking,^{37–39} were found in higher average levels in samples of PWH compared with PWoH (Figure S5D). However, none of these lipids reached significance at the selected statistical threshold of *p* < 0.05.

Histamine conjugates were linked to HIV status, while polyamine *N*-acyl lipids were associated with neurocognitive impairment status (impaired vs. unimpaired). Specifically, cadaverine and putrescine *N*-acyl lipids, particularly those with short acyl chains, were elevated in the impaired group compared with the unimpaired group (Mann-Whitney U test, *p* values from 0.001 to 0.04; Figures S5B and S5E). Further, analyses using a linear mixed-effects model, with fixed covariates of HIV status and neurocognitive impairment status, while treating the subject as a random effect, suggest that histamine-C2:0 and histamine-C3:0 continue to be positively associated with HIV status, and acylated polyamines were associated with neurocognitive impairment (Figure 3A). Within the PWH subgroup, *N*-acyl cadaverines consistently trended higher in the impaired group; however, none reached statistical significance (Figures S5C and S5F). We also observed a trend where the histamine conjugates with C2, C3, C4, and C5 were negatively associated with CD4⁺/CD8⁺ T cell ratio considering only the PWH subset, which is an indicator of immune system homeostasis.⁴⁰ In contrast, polyamines, particularly cadaverines linked to C2, C3, C5, C6, and C7, showed a positive correlation with the CD4⁺/CD8⁺ ratio in PWH (Figure 3B). One concern is the potential for spurious matches. However, the consistent observation of multiple *N*-acyl derivatives of the same head group trending in the same direction suggests otherwise, with an extremely low probability of occurring by chance (e.g., the probability of five matches to *N*-acyl cadaverines is 8.17×10^{-10}), making random matches unlikely. Additionally, we explored the relationships between *N*-acyl lipids and plasma HIV RNA viral loads in the PWH subset. We found that *N*-acyl lipids with short acyl chains were positively associated with higher viral loads, while those with longer acyl chains were linked to lower viral loads (Figure S5G).

(E and F) Volcano plots of mouse fecal pellets from a dataset publicly available (GNPS/MassIVE: MSV000080918),³¹ showing *N*-acyl lipids upregulated and downregulated upon different diets (E) and antibiotic treatment (F). The significant thresholds are marked by dotted lines in the volcano plot (*p* < 0.05 and log₂ fold change [FC] > 2 or < 2). Differential compounds between the groups were evaluated using the non-parametric two-sided Mann-Whitney U test, and *p* values were corrected for multiple comparisons using the Benjamini-Hochberg correction. Icons were obtained from Bioicons.com.

Related to Figures S3 and S4.



(legend on next page)

To validate their identities, we matched retention time and MS/MS in comparison to pure synthetic standards for 13 of these short-chain fatty acid-derived *N*-acyl lipids that are associated with HIV status (histamine-C2:0, -C3:0, -C4:0, -C5:0, and -C6:0), neurocognitive impairment status (cadaverine-C2:0, -C3:0, -C5:0, -C6:0, and -C7:0), and included dopamine-C2:0, serotonin-C2:0, and tryptophan-C3:0 in this validation of the annotations of neurotransmitter derivatives—even though they did not associate with neurocognitive impairment (Figure 3C). All the compounds matched both the retention times and the MS/MS spectra in the fecal samples, confirming their presence in the samples (Figures S5H and S5I). Quantification experiments revealed that many of these compounds are present at high biological levels, reaching micromolar (μ M) concentrations (Table S3). Although we do not yet understand the biology behind this variability, and many samples had concentrations below the limit of quantification, the highest concentrations of *N*-acyl histamines that we quantified were 93.8, 20.7, 7.0, and 2.7 ng/g of fecal sample for histamine-C2:0 through histamine-C5:0, respectively. Additionally, for the *N*-acyl cadaverines, we found the concentrations to be as high as 350.4, 126.7, 36.7, and 1.3 ng/g for cadaverine-C2:0, cadaverine-C3:0, cadaverine-C5:0, and cadaverine-C6:0, respectively. Dopamine-C2:0 was also quantified, with levels ranging from 0.0008 to 3.2 ng/g. While histamine-C6:0, cadaverine-C7:0, serotonin-C2:0, and tryptophan-C3:0 were matched with retention times and MS/MS, their concentrations were too low to be accurately quantified in the samples.

Microbial producers of HIV-associated histamine *N*-acyl lipids

Samples from the HNRC also underwent metagenomic sequencing, allowing us to perform correlation analyses to identify microbes potentially responsible for producing histamine and polyamine *N*-acyl lipids associated with HIV and neurocognitive status. Previous microbial cultures from this study produced cadaverine-C2:0 and cadaverine-C4:0 (Figure S3G). Microbe-MASST searches also confirmed that cadaverine *N*-acyl lipids have been observed in microbial monocultures (Figure 1C). However, no microbial *N*-acyl histamines were detected in either public data or our experiments, raising the question of whether histamine conjugates are microbially produced, and if so, which microorganisms may be responsible for their production.

To investigate this further and identify microbes potentially associated with *N*-acyl histamines, we conducted a multiomic

microbe-metabolite co-occurrence analysis using mmvec.⁴¹ We observed a strong trend of distinct microbe-metabolite co-occurrences between PWH and PWoH (Figure S5J). Higher microbial-metabolite co-occurrence probabilities were observed for histamine-C2:0 and histamine-C3:0 (Table S3). Ten microbial taxonomic orders also stood out for presenting several organisms that resulted in high co-occurrence probabilities with both histamine-C2:0 and histamine-C3:0 but with histamine-C2:0 exhibiting more high co-occurrences than histamine-C3:0 (Figure 3D).

Based on the multiomics analysis and availability of strains, we selected nine bacterial strains from these microbial orders for culturing and supplemented the media with histamine, cadaverine, and putrescine. After 72 h of culturing, we analyzed the samples using LC-MS/MS and matched them against the *N*-acyl lipids library (Figure 3E). We identified histamine-C2:0, histamine-C3:0, cadaverine-C2:0, and cadaverine-C3:0 in the cultures at 72 h, whereas these compounds were not detected at 0 h post-addition. This finding confirms that some microorganisms are capable of producing these *N*-acyl lipids. Specifically, cadaverine-C3:0 was observed in cultures of *Collinsella aerofaciens* ATCC 25986 and *Prevotella buccae* D17, while cadaverine-C2:0 was detected in extracts from these two microbes as well as in *Catenibacterium mitsuokai* DSM 15897 and *Holdemanella bififormis* DSM 3989. *Catenibacterium mitsuokai* DSM 15897 produced only histamine-C2:0, whereas *Collinsella aerofaciens* ATCC 25986, *Holdemanella bififormis* DSM 3989, and *Prevotella buccae* D17 produced both histamine-C2:0 and histamine-C3:0. *Dorea longicatena* DSM 13814 produced only histamine-C3:0. *Collinsella aerofaciens* ATCC 25986 produced the highest amount of histamine-C2:0, with a concentration of $1.905 \pm 0.302 \mu$ M in the extracts (Figure 3E; Table S3). The highest levels of histamine-C3:0 were observed in *Prevotella buccae* D17, with a concentration of $0.358 \pm 0.016 \mu$ M. Cadaverine-C2:0 and cadaverine-C3:0 were confirmed to be produced by specific microbes by MS/MS and retention time matching, but these compounds were present in lower concentrations in the extracts and could not be accurately quantified.

Immunomodulatory activity of *N*-acyl lipids

To further investigate the potential role of *N*-acyl lipids in immune function, we analyzed their effects on CD4⁺ T cells polarization by measuring the expression of key transcription factors: Foxp3⁺ (regulatory T cell [Treg]), Tbet⁺ (T helper 1 [Th1]), and ROR γ T⁺ (Th17) on day 0 and day 3. We co-cultured murine

Figure 3. *N*-Acyl lipids are correlated with HIV and neurocognitive impairment status and produced by microbes

(A) Forest plot illustrating the coefficient estimate of a linear mixed-effects model for individual *N*-acyl lipid species, with fixed covariates of HIV status (PWH, $n = 226$; PWoH, $n = 87$) and neurocognitive impairment status (impaired, $n = 151$; unimpaired, $n = 162$), accounting for random effects within individual samples/visit where stool samples were collected. Filled squares (HIV status) and circles (neurocognitive impairment status) with corresponding confidence intervals represent significant *N*-acyl lipid species. Faded circles and squares depict non-significant species. Each color represents a different head group.

(B) Bar plot showing the correlation coefficients of association between CD4/CD8 ratio and various *N*-acyl lipids in a subset of the PWH ($n = 171$) with available metadata. Red bars represent positive correlations, while blue bars represent negative correlations, as determined by linear regression models. The p values shown are nominal; adjusted p values (corrected for multiple comparisons using the Benjamini-Hochberg method) are available in Table S3.

(C) Structures of all *N*-acyl lipids confirmed in this study with pure synthetic standards.

(D) Network of the microbial taxonomic orders with co-occurrences >6.0 and shared between histamine-C2:0 and histamine-C3:0. Nodes colored in pink are the orders selected for culturing experiments.

(E) Concentrations of histamine-C2:0 and histamine-C3:0 in microbial extracts. Values in the y axis represent the amount of these compounds in micromolar (μ M) concentrations in the extracts. Cadaverine (C), putrescine (P), and histamine (H) were added to the medium.

Related to Figure S5.

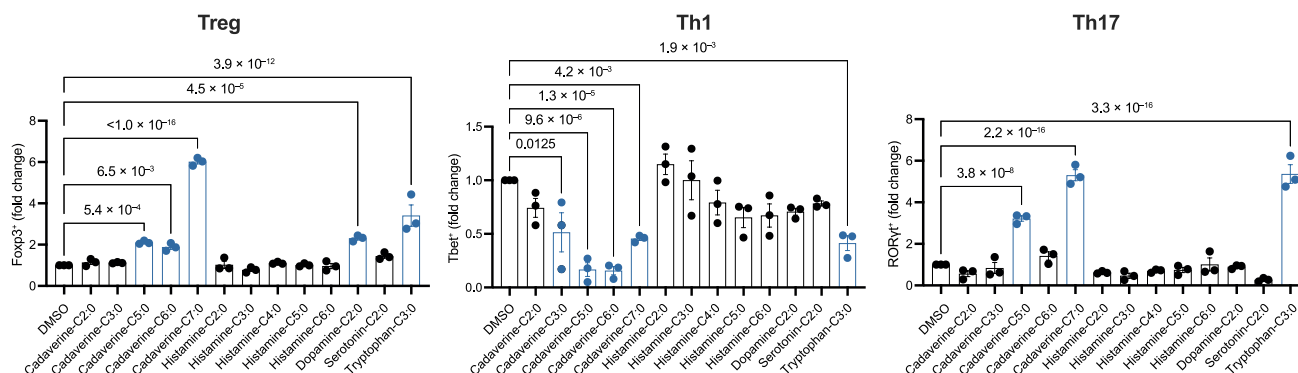


Figure 4. *N*-Acyl lipids have immunomodulatory activities

Flow cytometric quantification of Foxp3⁺ (left), Tbet⁺ (middle), and RORγT⁺ (right) induction in naive CD4⁺ T cells. Cells were treated with 100 μM of *N*-acyl lipids on day 0, and CD4⁺ T cells were gated for analyses on day 3. Data are representative of two independent experiments. Bar plot shows mean, and error bars represent SEM. One-way Dunnett's multiple comparisons test provided significance.

bone-marrow-derived dendritic cells and naive CD4⁺ T cells with pure *N*-acyl lipids (*N*-acyl histamines and cadaverines, dopamine-C2:0, serotonin-C2:0, and tryptophan-C3:0). Several *N*-acyl lipids exhibited distinct effects on T cell differentiation (Figure 4; Table S4). Cadaverine-C5:0, -C6:0, and -C7:0, as well as dopamine-C2:0 and tryptophan-C3:0, significantly increased Foxp3⁺ expression, suggesting a role in promoting Treg differentiation. In contrast, *N*-acyl cadaverines reduced Tbet⁺ expression in a lipid chain length-dependent manner, indicating a suppression of Th1 differentiation. Similarly, tryptophan-C3:0 also led to a reduction in Tbet⁺ expression. Additionally, cadaverine-C5:0, cadaverine-C7:0, and tryptophan-C3:0 significantly increased RORγT⁺ expression, suggesting a potential role in promoting Th17 differentiation. None of the *N*-acyl histamines or serotonin-C2:0 exhibited significant immunomodulatory effects under the tested conditions.

DISCUSSION

Despite their infrequent description or annotation in metabolomics data and literature, *N*-acyl lipids are quite prevalent, as revealed by our reverse metabolomics analysis using the MassQL-generated MS/MS reference resource. A significant portion of the *N*-acyl lipids identified in this study were derived from short-chain fatty acids. Free short-chain fatty acids are a key and extensively studied class of molecules produced at the microbiota-diet interface.⁴² While primarily produced in the gut, these fatty acids can impact distant organs such as the liver, lungs, urogenital tract, and brain.^{43–45} They play a role in immune regulation, affecting T cell functions and CD4⁺/CD8⁺ levels, and they are implicated in health conditions like disrupted intestinal barrier function and diseases, including autoimmune disorders, diabetes, and HIV.^{42,46,47}

Given the short-chain fatty acids prominence in microbiome research, it was surprising to find such a large panel of *N*-acyl lipids, many derived from short-chain fatty acids, which had not been previously documented in lipid structural data resources. Our study demonstrated that these *N*-acyl lipids are detected in data from sites distant from the gut. Their levels are

influenced by factors such as dietary changes, antibiotic use, and health conditions affecting the microbiome, such as diabetes, and by other microbiome-mediated processes such as decomposition. Additionally, analysis of publicly available data, along with microbial culturing experiments conducted in this study, showed that individual cultures can produce, in a microbe-specific manner, certain *N*-acyl lipids when both the amine head group and lipid substrates are present.

Data from fecal samples of PWH revealed a substantial number of microbially produced short-chain fatty acid-derived *N*-acyl lipids—an observation not previously identified despite numerous metabolomics studies on PWH.^{48–55} This discovery was made possible by the *N*-acyl lipid MS/MS resource created in this work. We found that microbially produced short-chain fatty acids linked to polyamines and histamine were associated with plasma HIV RNA viral load and CD4⁺/CD8⁺ levels in PWH. This study uncovered several *N*-acylated lipids related to HIV status, including histamine conjugates, while many polyamine-derived *N*-acyl lipids were associated with neurocognitive impairment status in both PWH and PWOh in this cohort.

Although limited information is available on histamine-containing *N*-acyl lipids, it is known that the non-acylated histamine itself, produced by macrophages, is increased in PWH.⁵⁶ Thus, one can hypothesize that the production of the *N*-acylated histamines may require not only the availability of histamine but also the short-chain fatty acids and the right organisms. Indeed, organisms such as *Prevotella*, which are commonly enriched in PWH,⁵⁷ can produce propionate from succinate⁵⁸ and have the ability to couple this to histamine. Beyond HIV populations, very little is known about the short-chain fatty acid-histamine conjugates. The C2 and C3 *N*-acyl histamines were previously found to be elevated in the urine of patients with intestinal disorders, and the histamine-C6 was found to be very modestly cytotoxic, while related molecules that have longer-chain fatty acids conjugated to them act on peroxisome proliferator-activated receptor-α (PPAR-α).^{59–61} PPAR-α protects from HIV-related systemic inflammation and improves intestinal barrier function.^{62,63} We did not find biological reports for the C4–C5

histamine conjugates, and it is not yet known if these specific *N*-acyl lipids also provide such protective effects.

There is a strong connection between HIV disease and polyamines. Polyamines, such as cadaverine, protect the HIV virion and sperm from the acidity in the vaginal tract and increase infectivity.⁶⁴ Polyamines are detected in higher quantities and affect Treg cell dysfunction in PWH.^{49,65,66} Intriguingly, polyamine metabolism plays a crucial role in maintaining the integrity of Th cell lineage, which is crucial in regulating inflammation and maintaining immune tolerance.^{67,68} As with the histamine conjugates, there is also limited information on polyamine conjugates and HIV disease or other health conditions. This includes the cadaverine *N*-acyl lipids, except for the commonly measured C2 conjugate, which has been associated with cancer and other health conditions, such as in the urine of individuals with Alzheimer's disease, and has been shown to reduce the aggressiveness of breast cancer in rodents.^{69–71} The cadaverine-C3, also known as *N*-propionyl cadaverine, has been shown to not only reach the brain of rats *in vivo* but also, as shown *in vitro*, to depress electrically stimulated dopamine release from the neostriatum from rats at concentrations in the nanomolar (nM) range.^{72–74} We did not find biological reports for the C4–C6 cadaverine, despite recent studies highlighting the discovery of microbiome-derived polyamines.^{23,75–77} We found that polyamine *N*-acyl lipids, especially cadaverine short-chain fatty acid conjugates, are associated with impairment status in this study. Although it is established that other polyamines, acetylspermidine, and unconjugated putrescine are biomarkers for HIV-associated neurocognitive disorders,⁷⁸ this is not known for the *N*-acyl-cadaverines.

Non-dietary histamine and cadaverine levels are reported to be inversely linked, and we see a similar trend for the *N*-acyl cadaverine and histamines and in relation to CD4⁺/CD8⁺ ratio. Although it is not yet known if *N*-acyl conjugates exhibit similar activities, cadaverine can potentiate histamine levels, possibly via competitive inhibition of histamine-degrading enzymes.^{79–81} This inverse relationship and the role of the *Prevotella*-derived production of short-chain fatty acid-linked histamine and polyamines and their role in HIV disease and HIV-associated neurocognitive impairment warrant more research. Additionally, since most participants in the study were on antiretroviral therapy, its potential impact on the *N*-acyl lipid levels should be further investigated. However, the *N*-acyl lipid reference resource from this work enabled the identification of previously detected but unannotated microbial-derived molecules and their associations with HIV disease and neurocognitive impairment.

HIV infection is known to cause loss of CD4⁺ T cells.⁸² A T-polarization assay revealed that specific *N*-acyl lipids observed in the HIV study, especially cadaverine conjugates, exhibit immunomodulatory effects by altering the expression of Treg, Th1, and Th17 cells, revealing activation and suppression. Although causal connections require further investigation, these expression patterns intriguingly align with previous observations of altered Treg, Th1, and Th17 responses in HIV, suggesting a potential role in balancing T cell dynamics.⁸³ The upregulation of Foxp3⁺, a marker for Treg, by cadaverine-C5:0, -C6:0, and -C7:0 suggests a potential role in immune activation. Th1 cells are important for antiviral immunity, including control of HIV repli-

cation, and their decline is a characteristic of HIV progression.⁸⁴ *N*-Acyl cadaverines induce a downregulation of Tbet⁺, the reporter for Th1, which suggests a shift toward an immunosuppressive state. The loss of Th17 cells in HIV is correlated with the decrease of the integrity of the gut mucosal barrier, which increases microbial translocation and, consequently, a systemic immune activation in HIV.⁸⁵ Cadaverine-C5:0 and -C7:0 were able to increase RORγt⁺ expression, restoring Th17 cells and promoting the mucosal barrier. T cells are able to cross the blood-brain barrier and are also associated with cognitive impairment.⁸⁶ Th17 cells have been correlated with increased cognitive impairment in stroke patients,^{87,88} while Th1 and Th17 were elevated in patients with Alzheimer's disease.⁸⁹ However, there is limited information on their role in cognitive impairment among PWH. In contrast to the *N*-acyl cadaverines, *N*-acyl histamines showed no immunomodulatory activity in the assays performed, and their potential biological functions in HIV, if any, remain unknown.

The unexpected discovery of hundreds of short-chain fatty acid-derived *N*-acyl lipids, not reported in structural lipid databases, highlights their widespread presence across all biofluids and organs for which data are available, despite several being produced by the microbiota. The identification of various structural family members opens an additional chapter in understanding the mechanistic and functional roles of short-chain fatty acids. This finding may even prompt a reinterpretation of how microbially produced short-chain fatty acids influence the production of *N*-acyl lipids and, consequently, a wide range of conditions, as they are only formed when both substrates are present and the appropriate microbe(s) is present to create the link. This resource has enabled the generation of numerous hypotheses regarding the functions of these *N*-acyl lipids, and we anticipate that fully elucidating their roles will require extensive research across many laboratories and thousands of studies.

While we provide signatures for 851 metabolites here, this is only the beginning. Many other amines are not covered in this study, and they also may be linked to different fatty acids. Lipids containing other atoms, such as oxygen, nitrogen, or halogens, were not included and would require dedicated MassQL queries or the development of alternative detection strategies. Alcohols might also undergo similar structural diversification. Moreover, the diversity of lipids available for acylation extends well beyond the C2:0 to C30:4 range of lipids we examined. We anticipate that this resource will spur the development of additional ways to find *N*-acyl lipids and will help uncover additional biological and health associations. This may enhance our understanding of microbiome-mediated effects and may potentially serve as easy-to-detect microbial biomarkers in precision medicine, given their prevalence. Finally, this resource captures the intersection of nutrient availability with microbial and host metabolism, warranting further exploration of their biological functions.

Limitations of the study

Users of this resource should consider three main limitations when making biological discoveries. First, while we have consistently matched the MS/MS of synthetic standards to MassQL-recovered spectra, there have been instances where the match

was to a different isomer. For example, in the cohort of the body decomposition study (Figures S4C and S4D), the *N*-acyl 2-phenethylamines matched both in retention time and MS/MS with the synthetic standard in the two chromatographic methods tested. However, even though the *N*-acyl amylamines MS/MS matched, the retention times were shifted by 0.1 min, suggesting the presence of a different isomer instead, such as a branched chain in the acyl portion. Even though this difference could arise due to matrix effects of the biological sample, co-migration analyses could confirm that these were indeed different compounds. Other head groups can also have more than one position for the acyl attachment, which will also result in very similar MS/MS spectra. For the HIV study, all the pure *N*-acyl lipid standards matched the compounds present in the samples. Even though there were three nitrogen atoms available for the acyl substitution, in the case of the *N*-acyl histamines, the substitution of the acyl chain was observed in the primary amine group in all instances. Therefore, at the repository-level search, it is advisable to refer to the number of carbons and double bonds in the lipid chain rather than to the exact structure, as multiple isomers can correspond to the same family of molecules (see Figure 1A).

Second, our initial query was designed to capture the protonated ion forms of the molecules. However, many different ion forms, such as adducts, multimers, and in/post-source fragments, are commonly detected for any given molecule. The fragmentation patterns of other ion forms may differ and would require separate MassQL queries. A limitation of using other ion forms for query development is the scarcity of reference spectra to understand their fragmentation behavior. Nevertheless, once an annotation is made, it is possible to retrieve associated MS/MS spectra for different ion forms through peak shape and retention time alignments.⁹⁰ Currently, this type of analysis is feasible only within a single dataset and not across all public data simultaneously.

Finally, it is crucial to note that our observations are based on the *N*-acyl lipid spectra detected in public-domain data. Reanalysis of public data allows for relative quantification; however, it is often important to know the exact amount that is detected. For example, if one wants to establish causal relationships, knowing the concentration is important. Biological associations can only be established when there are well-curated public (meta)data. Variations in underlying biological conditions—such as feeding time, health, circadian rhythm, and diet type—may affect concentrations and detectability in untargeted metabolomics. Moreover, mass spectrometry-based metabolomics data are highly sensitive to data acquisition parameters (e.g., mass spectrometer type, ionization technique, collision energies, chromatographic gradient) and sample preparation methodologies (e.g., storage conditions, extraction methods). In particular, the extraction efficiencies of *N*-acyl lipids were not systematically evaluated in this study, meaning that the reported quantifications represent a lower bound of their actual abundance in biological samples. Therefore, while the observed patterns and trends in *N*-acyl lipid distribution across various tissues and biofluids provide valuable insights, they should be interpreted with these considerations in mind, and the results should be used to formulate testable hypotheses.

RESOURCE AVAILABILITY

Lead contact

Further queries and reagent requests may be directed and will be fulfilled by the lead contact, Pieter C. Dorrestein (pdorrestein@health.ucsd.edu).

Materials availability

This study did not generate new unique reagents. All the reagents in this study were included in the [key resources table](#).

Data and code availability

The *N*-acyl lipids library is available as part of the GNPS public spectral libraries (<https://gnps.ucsd.edu/ProteoSAFe/gnpslibrary.jsp?library=GNPS-N-ACYL-LIPIDS-MASSQL>) and is also archived in Zenodo (<https://doi.org/10.5281/zenodo.14015198>). All the scripts used to perform the data analyses and generate the figures are available at https://github.com/helenamrusso/N-acyl_lipids. NMR data of the pure *N*-acyl lipids are archived at Zenodo (<https://doi.org/10.5281/zenodo.14015081>). All the untargeted metabolomics LC-MS/MS data are deposited on GNPS/MassIVE and are publicly available under the following accession numbers: MSV000088040 (monocolonized germ-free mice), MSV000082261 (diabetes), MSV000084322 (body decomposition, skin), and MSV000084463 (body decomposition, soil), MSV000080918 (diet and antibiotics treatment), MSV000095648 (microbial monocultures), MSV000092833 (HIV study), MSV000095423 (retention time and MS/MS matching), and MSV000096049 (method validation and quantification). Owing to human volunteer protection constraints, the sample metadata for the HNRC cohort will be provided upon request to HNRC: <https://hnrc.hivresearch.ucsd.edu/index.php/hnrc-home>.

ACKNOWLEDGMENTS

We thank the NIH (NIDDK) for supporting the development of tools for structure elucidation (R01DK136117) and the Collaborative Microbial Metabolite Center (U24DK133658), and the HIV Neurobehavioral Research Center (HNRC) is supported by center award P30MH062512 from NIMH. This work was further supported by BBSRC-NSF award 2152526. Research reported in this publication was supported in part by the National Center for Complementary and Integrative Health of the NIH under award number F32AT011475 to N.E.A. and by the Maternal and Pediatric Precision in Therapeutics project (P50HD106463). X.S. was supported by the National Key R&D Program of China (2022YFA0807300 and 2023YFA1800200), NSF of China (32270945), and STCSM (22ZR1468700 and 22140902400). S.L. was supported by Research Council of Finland funding (no. 363417). J.J.K. was supported by the NIH CTSA grant UL1TR001442 and the UCSD Microbiome Seed Grant. M.R. was supported by the NIH grant R37AI126277. G.T.W. was supported by the NIH training grant T32AI007036. G.J.N. was supported by the NIH fellowship F31AI186410. We also thank Dr. Jessica L. Metcalf for supervision of the human cadaver decomposition study and Dr. Robert Heaton for the participation in the development of the clinical cohort of HIV infection.

AUTHOR CONTRIBUTIONS

P.C.D. conceptualized the project. H.M.-R. and M.v.F. developed the MassQL queries and performed the repository-scale searches. H.M.-R. created the *N*-acyl lipid library. H.M.-R., S.L., W.D.G.N., L.K., P.R., H.N.Z., and P.W.P.G. performed data analysis. V.C.-L., G.T.W., G.J.N., L.C., C.W., and S.R. performed microbial incubation experiments. K.Z., M.R., and L.B. supervised the culturing experiments. H.M.-R., V.C.-L., W.D.G.N., J.Z., and M.J.M. acquired LC-MS/MS data. V.D., A.P., K.V., I.M., C.L., A.S., M.S., Y.L., and D.P. performed the combinatorial synthesis reactions. A.V.A., Y.T., and H.C. performed the immunomodulatory assays. P.C.D. and D.S. supervised the synthesis. M.S.A., R.J.E., D.J.M., J.E.I., D.F.Jr., and S.L. developed the clinical cohort of human immunodeficiency virus (HIV) infection. M.S.A. and C.X.W. assisted with data interpretation. Y.E.A. performed database searches. M.W. provided support for MassQL searches. X.S. and D.K. supervised the monocolonized mice study. J.J.K. and S.K. supervised the diabetes study. Z.B. supervised the human decomposition study. R.K. supervised sample

handling and DNA data acquisition for the HNRC cohort. H.M.-R. and P.C.D. drafted the manuscript. P.C.D. acquired funding and supervised this project. All authors reviewed and edited the manuscript.

DECLARATION OF INTERESTS

P.C.D. is an advisor and holds equity in Cybele, BileOmix, and Sirenas and is a scientific co-founder of, is an advisor to, and holds equity in Omata, Enveda, and Arome with prior approval by the University of California, San Diego. P.C.D. also consulted for DSM animal health in 2023. M.W. is a co-founder of Omata Labs LLC. R.K. is a scientific advisory board member of and consultant for BiomeSense, Inc., and has equity and receives income. He is a scientific advisory board member of and has equity in GenCirq. He is a consultant for DayTwo and receives income. He has equity in and acts as a consultant for Cybele. He is a co-founder of Biota, Inc., and has equity. He is a cofounder of Micronoma, has equity, and is a scientific advisory board member. The terms of these arrangements have been reviewed and approved by the University of California, San Diego, in accordance with its conflict-of-interest policies.

STAR★METHODS

Detailed methods are provided in the online version of this paper and include the following:

- [KEY RESOURCES TABLE](#)
- [EXPERIMENTAL MODEL AND STUDY PARTICIPANT DETAILS](#)
 - Bacterial culture conditions
 - Human fecal material
- [METHOD DETAILS](#)
 - Searches in LIPID MAPS
 - Design of the MassQL queries and creation of the *N*-acyl lipids library
 - *N*-acyl lipids repository-scale search
 - Reanalysis of public data from GNPS/MassIVE
 - Bacterial cultures screening
 - Combinatorial reactions of *N*-acyl lipids
 - HIV Neurobehavioral Research Center (HNRC) cohort study
 - Immunomodulatory Activity assays
- [QUANTIFICATION AND STATISTICAL ANALYSIS](#)
 - Source of the pure *N*-acyl lipids
 - Quantification of *N*-acyl lipids in biological samples
 - Statistical analyses

SUPPLEMENTAL INFORMATION

Supplemental information can be found online at <https://doi.org/10.1016/j.cell.2025.05.015>.

Received: November 1, 2024

Revised: March 12, 2025

Accepted: May 16, 2025

Published: June 10, 2025

REFERENCES

1. Chang, F.-Y., Siuti, P., Laurent, S., Williams, T., Glassey, E., Sailer, A.W., Gordon, D.B., Hemmerle, H., and Voigt, C.A. (2021). Gut-inhabiting Clostridia build human GPCR ligands by conjugating neurotransmitters with diet- and human-derived fatty acids. *Nat. Microbiol.* 6, 792–805. <https://doi.org/10.1038/s41564-021-00887-y>.
2. Mann, A., Smoum, R., Trembovier, V., Alexandrovich, A., Breuer, A., Mechoulam, R., and Shohami, E. (2015). Palmitoyl Serine: An Endogenous Neuroprotective Endocannabinoid-Like Entity After Traumatic Brain Injury. *J. Neuroimmune Pharmacol.* 10, 356–363. <https://doi.org/10.1007/s11481-015-9595-z>.
3. Waluk, D.P., Vielfort, K., Derakhshan, S., Aro, H., and Hunt, M.C. (2013). N-Acyl taurines trigger insulin secretion by increasing calcium flux in pancreatic β -cells. *Biochem. Biophys. Res. Commun.* 430, 54–59. <https://doi.org/10.1016/j.bbrc.2012.11.026>.
4. Aichler, M., Borgmann, D., Krumsiek, J., Buck, A., MacDonald, P.E., Fox, J.E.M., Lyon, J., Light, P.E., Keipert, S., Jastroch, M., et al. (2017). N-acyl Taurines and Acylcarnitines Cause an Imbalance in Insulin Synthesis and Secretion Provoking β Cell Dysfunction in Type 2 Diabetes. *Cell Metab.* 25, 1334–1347. <https://doi.org/10.1016/j.cmet.2017.04.012>.
5. Arul Prakash, S., and Kamlekar, R.K. (2021). Function and therapeutic potential of N-acyl amino acids. *Chem. Phys. Lipids* 239, 105114. <https://doi.org/10.1016/j.chemphyslip.2021.105114>.
6. Long, J.Z., Svensson, K.J., Bateman, L.A., Lin, H., Kamenecka, T., Lokurkar, I.A., Lou, J., Rao, R.R., Chang, M.R., Jedrychowski, M.P., et al. (2016). The secreted enzyme PM20D1 regulates lipidated amino acid uncouplers of mitochondria. *Cell* 166, 424–435. <https://doi.org/10.1016/j.cell.2016.05.071>.
7. Connor, M., Vaughan, C.W., and Vandenberg, R.J. (2010). N-acyl amino acids and N-acyl neurotransmitter conjugates: neuromodulators and probes for new drug targets. *Br. J. Pharmacol.* 160, 1857–1871. <https://doi.org/10.1111/j.1476-5381.2010.00862.x>.
8. Jørgensen, A.M., Wibbel, R., and Bernkop-Schnürch, A. (2023). Biodegradable cationic and ionizable cationic lipids: A roadmap for safer pharmaceutical excipients. *Small* 19, e2206968. <https://doi.org/10.1002/smll.202206968>.
9. Mokhtari, V., Afsharian, P., Shahhoseini, M., Kalantar, S.M., and Moini, A. (2017). A review on various uses of N-acetyl cysteine. *Cell J.* 19, 11–17. <https://doi.org/10.22074/cellj.2016.4872>.
10. Conroy, M.J., Andrews, R.M., Andrews, S., Cockayne, L., Dennis, E.A., Fahy, E., Gaud, C., Griffiths, W.J., Jukes, G., Kolchin, M., et al. (2024). LIPID MAPS: update to databases and tools for the lipidomics community. *Nucleic Acids Res.* 52, D1677–D1682. <https://doi.org/10.1093/nar/gkad896>.
11. Xue, J., Chi, L., Tu, P., Lai, Y., Liu, C.-W., Ru, H., and Lu, K. (2021). Detection of gut microbiota and pathogen produced N-acyl homoserine in host circulation and tissues. *NPJ Biofilms Microbiomes* 7, 53. <https://doi.org/10.1038/s41522-021-00224-5>.
12. Tan, B., O'Dell, D.K., Yu, Y.W., Monn, M.F., Hughes, H.V., Burstein, S., and Walker, J.M. (2010). Identification of endogenous acyl amino acids based on a targeted lipidomics approach. *J. Lipid Res.* 51, 112–119. <https://doi.org/10.1194/jlr.M900198-JLR200>.
13. Wood, P.L. (2019). Targeted lipidomics and metabolomics evaluations of cortical neuronal stress in schizophrenia. *Schizophr. Res.* 212, 107–112. <https://doi.org/10.1016/j.schres.2019.08.003>.
14. Gentry, E.C., Collins, S.L., Panitchpakdi, M., Belda-Ferre, P., Stewart, A. K., Carrillo Terrazas, M., Lu, H.-H., Zuffa, S., Yan, T., Avila-Pacheco, J., et al. (2024). Reverse metabolomics for the discovery of chemical structures from humans. *Nature* 626, 419–426. <https://doi.org/10.1038/s41586-023-06906-8>.
15. Charron-Lamoureux, V., Mannocho-Russo, H., Lamichhane, S., Xing, S., Patan, A., Portal Gomes, P.W., Rajkumar, P., Deleray, V., Caraballo-Rodríguez, A.M., Chua, K.V., et al. (2025). A guide to reverse metabolomics—a framework for big data discovery strategy. *Nat. Protoc.*, 1–34. <https://doi.org/10.1038/s41596-024-01136-2>.
16. Zuffa, S., Schmid, R., Bauermeister, A., P Gomes, P.W., Caraballo-Rodríguez, A.M., El Abiead, Y., Aron, A.T., Gentry, E.C., Zemlin, J., Meehan, M. J., et al. (2024). microbeMASST: a taxonomically informed mass spectrometry search tool for microbial metabolomics data. *Nat. Microbiol.* 9, 336–345. <https://doi.org/10.1038/s41564-023-01575-9>.
17. West, K.A., Schmid, R., Gauglitz, J.M., Wang, M., and Dorrestein, P.C. (2022). foodMASST a mass spectrometry search tool for foods and beverages. *NPJ Sci. Food* 6, 22. <https://doi.org/10.1038/s41538-022-00137-3>.

18. Gomes, P.W.P., Mannochio-Russo, H., Schmid, R., Zuffa, S., Damiani, T., Quiros-Guerrero, L.-M., Caraballo-Rodríguez, A.M., Zhao, H.N., Yang, H., Xing, S., et al. (2024). plantMASST - Community-driven chemotaxonomic digitization of plants. Preprint at bioRxiv, 2024.05.13.593988. <https://doi.org/10.1101/2024.05.13.593988>.
19. Wang, M., Jarmusch, A.K., Vargas, F., Aksenov, A.A., Gauglitz, J.M., Weldon, K., Petras, D., da Silva, R., Quinn, R., Melnik, A.V., et al. (2020). Mass spectrometry searches using MASST. *Nat. Biotechnol.* 38, 23–26. <https://doi.org/10.1038/s41587-019-0375-9>.
20. Jarmusch, A.K., Wang, M., Aceves, C.M., Advani, R.S., Aguirre, S., Aksenov, A.A., Aleti, G., Aron, A.T., Bauermeister, A., Bolledu, S., et al. (2020). ReDU: a framework to find and reanalyze public mass spectrometry data. *Nat. Methods* 17, 901–904. <https://doi.org/10.1038/s41592-020-0916-7>.
21. Damiani, T., Jarmusch, A.K., Aron, A.T., Petras, D., Phelan, V.V., Zhao, H.N., Bittremieux, W., Acharya, D.D., Ahmed, M.M.A., Bauermeister, A., et al. (2025). A Universal Language for Finding Mass Spectrometry Data Patterns. *Nat. Methods*, 1–8. <https://doi.org/10.1038/s41592-025-02660-z>.
22. Wang, M., Carver, J.J., Phelan, V.V., Sanchez, L.M., Garg, N., Peng, Y., Nguyen, D.D., Watrous, J., Kapono, C.A., Luzzatto-Knaan, T., et al. (2016). Sharing and community curation of mass spectrometry data with Global Natural Products Social Molecular Networking. *Nat. Biotechnol.* 34, 828–837. <https://doi.org/10.1038/nbt.3597>.
23. Mohanty, I., Mannochio-Russo, H., Schweer, J.V., El Abiad, Y., Bittremieux, W., Xing, S., Schmid, R., Zuffa, S., Vasquez, F., Muti, V.B., et al. (2024). The underappreciated diversity of bile acid modifications. *Cell* 187, 1801–1818. <https://doi.org/10.1016/j.cell.2024.02.019>.
24. Watanabe, K., Yasugi, E., and Oshima, M. (2000). How to search the glycolipid data in “LIPIDBANK for web” the newly developed lipid database in Japan. *Trends Glycosci. Glycotechnol.* 12, 175–184. <https://doi.org/10.4052/tigg.12.175>.
25. Aimo, L., Liechti, R., Hyka-Nouspikel, N., Niknejad, A., Gleizes, A., Götz, L., Kuznetsov, D., David, F.P.A., van der Goot, F.G., Riezman, H., et al. (2015). The SwissLipids knowledgebase for lipid biology. *Bioinformatics* 31, 2860–2866. <https://doi.org/10.1093/bioinformatics/btv285>.
26. Bhandari, S., Bisht, K.S., and Merkler, D.J. (2021). The Biosynthesis and Metabolism of the N-Acylated Aromatic Amino Acids: N-Acylphenylalanine, N-Acyltyrosine, N-Acyltryptophan, and N-Acylhistidine. *Front. Mol. Biosci.* 8, 801749. <https://doi.org/10.3389/fmolb.2021.801749>.
27. Ghosh, A.K., and Shahabi, D. (2021). Synthesis of amide derivatives for electron deficient amines and functionalized carboxylic acids using EDC and DMAP and a catalytic amount of HOBt as the coupling reagents. *Tetrahedron Lett.* 63, 152719. <https://doi.org/10.1016/j.tetlet.2020.152719>.
28. Sumner, L.W., Amberg, A., Barrett, D., Beale, M.H., Beger, R., Daykin, C.A., Fan, T.W.-M., Fiehn, O., Goodacre, R., Griffin, J.L., et al. (2007). Proposed minimum reporting standards for chemical analysis Chemical Analysis Working Group (CAWG) Metabolomics Standards Initiative (MSI). *Metabolomics* 3, 211–221. <https://doi.org/10.1007/s11306-007-0082-2>.
29. Schymanski, E.L., Jeon, J., Gulde, R., Fenner, K., Ruff, M., Singer, H.P., and Hollender, J. (2014). Identifying small molecules via high resolution mass spectrometry: communicating confidence. *Environ. Sci. Technol.* 48, 2097–2098. <https://doi.org/10.1021/es5002105>.
30. Batsoyol, N., Pullman, B., Wang, M., Bandeira, N., and Swanson, S. (2022). P-Massive: A Real-Time Search Engine for a Multi-Terabyte Mass Spectrometry Database. In *International Conference for High Performance Computing, Networking, Storage and Analysis*, pp. 1–15. <https://doi.org/10.1109/SC41404.2022.00014>.
31. Shalapour, S., Lin, X.-J., Bastian, I.N., Brain, J., Burt, A.D., Aksenov, A.A., Vrbanc, A.F., Li, W., Perkins, A., Matsutani, T., et al. (2017). Inflammation-induced IgA+ cells dismantle anti-liver cancer immunity. *Nature* 551, 340–345. <https://doi.org/10.1038/nature24302>.
32. Song, X., Zhang, H., Zhang, Y., Goh, B., Bao, B., Mello, S.S., Sun, X., Zheng, W., Gazzaniga, F.S., Wu, M., et al. (2023). Gut microbial fatty acid isomerization modulates intraepithelial T cells. *Nature* 619, 837–843. <https://doi.org/10.1038/s41586-023-06265-4>.
33. Wu, M., Zheng, W., Song, X., Bao, B., Wang, Y., Ramanan, D., Yang, D., Liu, R., Macbeth, J.C., Do, E.A., et al. (2024). Gut complement induced by the microbiota combats pathogens and spares commensals. *Cell* 187, 897–913. <https://doi.org/10.1016/j.cell.2023.12.036>.
34. Cheng, J., Venkatesh, S., Ke, K., Barratt, M.J., and Gordon, J.I. (2024). A human gut *Faecalibacterium prausnitzii* fatty acid amide hydrolase. *Science* 386, eado6828. <https://doi.org/10.1126/science.ado6828>.
35. Cheng, A.G., Ho, P.-Y., Aranda-Díaz, A., Jain, S., Yu, F.B., Meng, X., Wang, M., Iakiviak, M., Nagashima, K., Zhao, A., et al. (2022). Design, construction, and in vivo augmentation of a complex gut microbiome. *Cell* 185, 3617–3636. <https://doi.org/10.1016/j.cell.2022.08.003>.
36. Burcham, Z.M., Belk, A.D., McGivern, B.B., Bouslimani, A., Ghadermazi, P., Martino, C., Shenav, L., Zhang, A.R., Shi, P., Emmons, A., et al. (2024). A conserved interdomain microbial network underpins cadaver decomposition despite environmental variables. *Nat. Microbiol.* 9, 595–613. <https://doi.org/10.1038/s41564-023-01580-y>.
37. Watrous, J., Roach, P., Alexandrov, T., Heath, B.S., Yang, J.Y., Kersten, R.D., van der Voort, M., Pogliano, K., Gross, H., Raaijmakers, J.M., et al. (2012). Mass spectral molecular networking of living microbial colonies. *Proc. Natl. Acad. Sci. USA* 109, E1743–E1752. <https://doi.org/10.1073/pnas.1203689109>.
38. Quinn, R.A., Melnik, A.V., Vrbanc, A., Fu, T., Patras, K.A., Christy, M.P., Bodai, Z., Belda-Ferre, P., Tripathi, A., Chung, L.K., et al. (2020). Global chemical effects of the microbiome include new bile-acid conjugations. *Nature* 579, 123–129. <https://doi.org/10.1038/s41586-020-2047-9>.
39. Quinn, R.A., Nothias, L.-F., Vining, O., Meehan, M., Esquenazi, E., and Dorrestein, P.C. (2017). Molecular networking as a drug discovery, drug metabolism, and precision medicine strategy. *Trends Pharmacol. Sci.* 38, 143–154. <https://doi.org/10.1016/j.tips.2016.10.011>.
40. Buggert, M., Frederiksen, J., Noyan, K., Svård, J., Barqasho, B., Sönnernborg, A., Lund, O., Nowak, P., and Karlsson, A.C. (2014). Multiparametric bioinformatics distinguish the CD4/CD8 ratio as a suitable laboratory predictor of combined T cell pathogenesis in HIV infection. *J. Immunol.* 192, 2099–2108. <https://doi.org/10.4049/jimmunol.1302596>.
41. Morton, J.T., Aksenov, A.A., Nothias, L.F., Foulds, J.R., Quinn, R.A., Badri, M.H., Swenson, T.L., Van Goethem, M.W., Northen, T.R., Vazquez-Baeza, Y., et al. (2019). Learning representations of microbe-metabolite interactions. *Nat. Methods* 16, 1306–1314. <https://doi.org/10.1038/s41592-019-0616-3>.
42. Mann, E.R., Lam, Y.K., and Uhlig, H.H. (2024). Short-chain fatty acids: linking diet, the microbiome and immunity. *Nat. Rev. Immunol.* 24, 577–595. <https://doi.org/10.1038/s41577-024-01014-8>.
43. Silva, Y.P., Bernardi, A., and Frozza, R.L. (2020). The role of short-chain fatty acids from gut Microbiota in gut-brain communication. *Front. Endocrinol.* 11, 25. <https://doi.org/10.3389/fendo.2020.00025>.
44. van der Hee, B., and Wells, J.M. (2021). Microbial regulation of host physiology by short-chain fatty acids. *Trends Microbiol.* 29, 700–712. <https://doi.org/10.1016/j.tim.2021.02.001>.
45. Verma, A., Bhagchandani, T., Rai, A., Nikita, S., Bhavesh, U.K., NS, Gulati, S., Malik, R., and Tandon, R. (2024). Short-chain fatty acid (SCFA) as a connecting link between Microbiota and gut-lung axis-A potential therapeutic intervention to improve lung health. *ACS Omega* 9, 14648–14671.
46. González-Hernández, L.A., Ruiz-Briseño, M.D.R., Sánchez-Reyes, K., Alvarez-Zavala, M., Vega-Magaña, N., López-Iñiguez, A., Díaz-Ramos, J.A., Martínez-Ayala, P., Soria-Rodríguez, R.A., Ramos-Solano, M., et al. (2019). Alterations in bacterial communities, SCFA and biomarkers in an elderly HIV-positive and HIV-negative population in western Mexico. *BMC Infect. Dis.* 19, 234. <https://doi.org/10.1186/s12879-019-3867-9>.

47. Enriquez, A.B., Ten Caten, F., Ghneim, K., Sekaly, R.-P., and Sharma, A. A. (2023). Regulation of immune homeostasis, inflammation, and HIV persistence by the microbiome, short-chain fatty acids, and bile acids. *Annu. Rev. Virol.* 10, 397–422. <https://doi.org/10.1146/annurev-virology-040323-082822>.
48. Hollenbaugh, J.A., Munger, J., and Kim, B. (2011). Metabolite profiles of human immunodeficiency virus infected CD4+ T cells and macrophages using LC-MS/MS analysis. *Virology* 415, 153–159. <https://doi.org/10.1016/j.virol.2011.04.007>.
49. Mahalingam, S.S., Jayaraman, S., Bhaskaran, N., Schneider, E., Fadoul, F., Paes da Silva, A., Lederman, M.M., Asaad, R., Adkins-Travis, K., Shriver, L.P., et al. (2023). Polyamine metabolism impacts T cell dysfunction in the oral mucosa of people living with HIV. *Nat. Commun.* 14, 399. <https://doi.org/10.1038/s41467-023-36163-2>.
50. Moon, J.-Y., Zolnik, C.P., Wang, Z., Qiu, Y., Usyk, M., Wang, T., Kizer, J. R., Landay, A.L., Kurland, I.J., Anastos, K., et al. (2018). Gut microbiota and plasma metabolites associated with diabetes in women with, or at high risk for, HIV infection. *EBiomedicine* 37, 392–400. <https://doi.org/10.1016/j.ebiom.2018.10.037>.
51. Li, X., Wu, T., Jiang, Y., Zhang, Z., Han, X., Geng, W., Ding, H., Kang, J., Wang, Q., and Shang, H. (2018). Plasma metabolic changes in Chinese HIV-infected patients receiving lopinavir/ritonavir based treatment: Implications for HIV precision therapy. *Cytokine* 110, 204–212. <https://doi.org/10.1016/j.cyto.2018.05.001>.
52. Ding, Y., Lin, H., Chen, X., Zhu, B., Xu, X., Xu, X., Shen, W., Gao, M., and He, N. (2021). Comprehensive metabolomics profiling reveals common metabolic alterations underlying the four major non-communicable diseases in treated HIV infection. *EBiomedicine* 71, 103548. <https://doi.org/10.1016/j.ebiom.2021.103548>.
53. Cassol, E., Misra, V., Holman, A., Kamat, A., Morgello, S., and Gabuzda, D. (2013). Plasma metabolomics identifies lipid abnormalities linked to markers of inflammation, microbial translocation, and hepatic function in HIV patients receiving protease inhibitors. *BMC Infect. Dis.* 13, 203. <https://doi.org/10.1186/1471-2334-13-203>.
54. Babu, H., Sperk, M., Ambikan, A.T., Rachel, G., Viswanathan, V.K., Tripathy, S.P., Nowak, P., Hanna, L.E., and Neogi, U. (2019). Plasma metabolic signature and abnormalities in HIV-infected individuals on long-term successful antiretroviral therapy. *Metabolites* 9, 210. <https://doi.org/10.3390/metabo9100210>.
55. Taylor, B.C., Weldon, K.C., Ellis, R.J., Franklin, D., Groth, T., Gentry, E.C., Tripathi, A., McDonald, D., Humphrey, G., Bryant, M., et al. (2020). Depression in individuals coinfecting with HIV and HCV is associated with systematic differences in the gut microbiome and metabolome. *mSystems* 5, e0046520. <https://doi.org/10.1128/mSystems.00465-20>.
56. Pedersen, M., Nielsen, C.M., and Permin, H. (1991). HIV antigen-induced release of histamine from basophils from HIV infected patients. Mechanism and relation to disease progression and immunodeficiency. *Allergy* 46, 206–212. <https://doi.org/10.1111/j.1398-9995.1991.tb00572.x>.
57. Armstrong, A.J.S., Shaffer, M., Nusbacher, N.M., Griesmer, C., Fiorillo, S., Schneider, J.M., Preston Neff, C., Li, S.X., Fontenot, A.P., Campbell, T., et al. (2018). An exploration of Prevotella-rich microbiomes in HIV and men who have sex with men. *Microbiome* 6, 198. <https://doi.org/10.1186/s40168-018-0580-7>.
58. Fusco, W., Lorenzo, M.B., Cintoni, M., Porcari, S., Rinninella, E., Kaitsas, F., Lener, E., Mele, M.C., Gasbarrini, A., Collado, M.C., et al. (2023). Short-chain fatty-acid-producing bacteria: Key components of the human gut Microbiota. *Nutrients* 15, 2211. <https://doi.org/10.3390/nu15092211>.
59. Hövelmann, Y., Steinert, K., Hübner, F., and Humpf, H.-U. (2020). Identification of a novel N-caprylhistamine- β -glucoside from tomato fruits and LC-MS/MS-based food screening for imidazole alkaloids. *Food Chem.* 312, 126068. <https://doi.org/10.1016/j.foodchem.2019.126068>.
60. Hövelmann, Y., Hahn, M., Hübner, F., and Humpf, H.-U. (2019). Detection of novel cytotoxic imidazole alkaloids in tomato products by LC-MS/MS. *J. Agric. Food Chem.* 67, 3670–3678. <https://doi.org/10.1021/acs.jafc.9b00461>.
61. Takao, K., Noguchi, K., Hashimoto, Y., Shirahata, A., and Sugita, Y. (2015). Synthesis and evaluation of fatty acid amides on the N-oleoylethanolamide-like activation of peroxisome proliferator activated receptor α . *Chem. Pharm. Bull.* 63, 278–285. <https://doi.org/10.1248/cpb.c14-00881>.
62. Huang, W., Rha, G.B., Han, M.-J., Eum, S.Y., András, I.E., Zhong, Y., Hennig, B., and Toborek, M. (2008). PPAR α and PPAR γ effectively protect against HIV-induced inflammatory responses in brain endothelial cells. *J. Neurochem.* 107, 497–509. <https://doi.org/10.1111/j.1471-4159.2008.05626.x>.
63. Crakes, K.R., Santos Rocha, C., Grishina, I., Hirao, L.A., Napoli, E., Gaulke, C.A., Fenton, A., Datta, S., Arredondo, J., Marco, M.L., et al. (2019). PPAR α -targeted mitochondrial bioenergetics mediate repair of intestinal barriers at the host-microbe intersection during SIV infection. *Proc. Natl. Acad. Sci. USA* 116, 24819–24829. <https://doi.org/10.1073/pnas.1908977116>.
64. Roan, N.R., and Greene, W.C. (2007). A seminal finding for understanding HIV transmission. *Cell* 131, 1044–1046. <https://doi.org/10.1016/j.cell.2007.11.030>.
65. Herbert, C., Luies, L., Loots, D.T., and Williams, A.A. (2023). The metabolic consequences of HIV/TB co-infection. *BMC Infect. Dis.* 23, 536. <https://doi.org/10.1186/s12879-023-08505-4>.
66. Zhang, Y., Xie, Z., Zhou, J., Li, Y., Ning, C., Su, Q., Ye, L., Ai, S., Lai, J., Pan, P., et al. (2022). The altered metabolites contributed by dysbiosis of gut microbiota are associated with microbial translocation and immune activation during HIV infection. *Front. Immunol.* 13, 1020822. <https://doi.org/10.3389/fimmu.2022.1020822>.
67. Wu, R., Chen, X., Kang, S., Wang, T., Gnanaprakasam, J.R., Yao, Y., Liu, L., Fan, G., Burns, M.R., and Wang, R. (2020). De novo synthesis and salvage pathway coordinately regulate polyamine homeostasis and determine T cell proliferation and function. *Sci. Adv.* 6, eabc4275. <https://doi.org/10.1126/sciadv.abc4275>.
68. Puleston, D.J., Baixauli, F., Sanin, D.E., Edwards-Hicks, J., Villa, M., Kambat, A.M., Kamiński, M.M., Stanckzak, M., Weiss, H.J., Grzes, K.M., et al. (2021). Polyamine metabolism is a central determinant of helper T cell lineage fidelity. *Cell* 184, 4186–4202. <https://doi.org/10.1016/j.cell.2021.06.007>.
69. Lee, S.H., Kim, S.O., Lee, H.D., and Chung, B.C. (1998). Estrogens and polyamines in breast cancer: their profiles and values in disease staging. *Cancer Lett.* 133, 47–56. [https://doi.org/10.1016/s0304-3835\(98\)00189-x](https://doi.org/10.1016/s0304-3835(98)00189-x).
70. Paik, M.-J., Lee, S., Cho, K.-H., and Kim, K.-R. (2006). Urinary polyamines and N-acetylated polyamines in four patients with Alzheimer's disease as their N-ethoxycarbonyl-N-pentafluoropropionyl derivatives by gas chromatography-mass spectrometry in selected ion monitoring mode. *Anal. Chim. Acta* 576, 55–60. <https://doi.org/10.1016/j.aca.2006.01.070>.
71. Kovács, T., Mikó, E., Vida, A., Sebő, É., Toth, J., Csonka, T., Boratkó, A., Ujlaki, G., Lente, G., Kovács, P., et al. (2019). Cadaverine, a metabolite of the microbiome, reduces breast cancer aggressiveness through trace amino acid receptors. *Sci. Rep.* 9, 1300. <https://doi.org/10.1038/s41598-018-37664-7>.
72. Salzman, S.K., and Stepita-Klauco, M. (1981). Inhibition of evoked dopamine release by monopropanolcadaverine in vitro. *Pharmacol. Biochem. Behav.* 15, 119–123. [https://doi.org/10.1016/0091-3057\(81\)90349-x](https://doi.org/10.1016/0091-3057(81)90349-x).
73. Murray, K.E., Shaw, K.J., Adams, R.F., and Conway, P.L. (1993). Presence of N-acyl and acetoxyl derivatives of putrescine and cadaverine in the human gut. *Gut* 34, 489–493. <https://doi.org/10.1136/gut.34.4.489>.
74. Salzman, S.K., and Stepita-Klauco, M. (1981). Cadaverine in the rat brain: regional distribution and acylation of [^{14}C]cadaverine in vivo and uptake in vitro. *J. Neurochem.* 37, 1308–1315. <https://doi.org/10.1111/j.1471-4159.1981.tb04682.x>.

75. Mayers, J.R., Varon, J., Zhou, R.R., Daniel-Ivad, M., Beaulieu, C., Bhosle, A., Glasser, N.R., Lichtenauer, F.M., Ng, J., Vera, M.P., et al. (2024). A metabolomics pipeline highlights microbial metabolism in bloodstream infections. *Cell* 187, 4095–4112. <https://doi.org/10.1016/j.cell.2024.05.035>.
76. Dudkina, N., Park, H.B., Song, D., Jain, A., Khan, S.A., Flavell, R.A., Johnson, C.H., Palm, N.W., and Crawford, J.M. (2024). Human AKR1C3 binds agonists of GPR84 and participates in an expanded polyamine pathway. *Cell Chem. Biol.* 32, 126–144. <https://doi.org/10.1016/j.chembiol.2024.07.011>.
77. Elmassry, M.M., Sugihara, K., Chankhamjon, P., Kim, Y., Camacho, F.R., Wang, S., Sugimoto, Y., Chatterjee, S., Chen, L.A., Kamada, N., et al. (2025). A meta-analysis of the gut microbiome in inflammatory bowel disease patients identifies disease-associated small molecules. *Cell Host Microbe* 33, 218–234. <https://doi.org/10.1016/j.chom.2025.01.002>.
78. Merali, S., Barrero, C.A., Sacktor, N.C., Haughey, N.J., Datta, P.K., Langford, D., and Khalili, K. (2014). Polyamines: Predictive biomarker for HIV-associated neurocognitive disorders. *J. AIDS Clin. Res.* 5, 1000312. <https://doi.org/10.4172/2155-6113.1000312>.
79. Lyons, D.E., Beery, J.T., Lyons, S.A., and Taylor, S.L. (1983). Cadaverine and aminoguanidine potentiate the uptake of histamine in vitro in perfused intestinal segments of rats. *Toxicol. Appl. Pharmacol.* 70, 445–458. [https://doi.org/10.1016/0041-008x\(83\)90162-x](https://doi.org/10.1016/0041-008x(83)90162-x).
80. Sánchez-Pérez, S., Comas-Basté, O., Costa-Catala, J., Iduriaga-Platero, I., Veciana-Nogués, M.T., Vidal-Carou, M.C., and Latorre-Moratalla, M.L. (2022). The rate of histamine degradation by diamine oxidase is compromised by other biogenic amines. *Front. Nutr.* 9, 897028. <https://doi.org/10.3389/fnut.2022.897028>.
81. Hui, J.Y., and Taylor, S.L. (1985). Inhibition of in vivo histamine metabolism in rats by foodborne and pharmacologic inhibitors of diamine oxidase, histamine N-methyltransferase, and monoamine oxidase. *Toxicol. Appl. Pharmacol.* 81, 241–249. [https://doi.org/10.1016/0041-008x\(85\)90160-7](https://doi.org/10.1016/0041-008x(85)90160-7).
82. Douek, D.C., Picker, L.J., and Koup, R.A. (2003). T cell dynamics in HIV-1 infection. *Annu. Rev. Immunol.* 21, 265–304. <https://doi.org/10.1146/annurev.immunol.21.120601.141053>.
83. López-Abente, J., Correa-Rocha, R., and Pion, M. (2016). Functional mechanisms of Treg in the context of HIV infection and the Janus face of immune suppression. *Front. Immunol.* 7, 192. <https://doi.org/10.3389/fimmu.2016.00192>.
84. Langford, S.E., Ananworanich, J., and Cooper, D.A. (2007). Predictors of disease progression in HIV infection: a review. *AIDS Res. Ther.* 4, 11. <https://doi.org/10.1186/1742-6405-4-11>.
85. Renault, C., Veyrenche, N., Mennechet, F., Bedin, A.-S., Routy, J.-P., Van de Perre, P., Reynes, J., and Tuaillon, E. (2022). Th17 CD4+ T-cell as a preferential target for HIV reservoirs. *Front. Immunol.* 13, 822576. <https://doi.org/10.3389/fimmu.2022.822576>.
86. Ruiz-Fernández, I., Sánchez-Díaz, R., Ortega-Sollero, E., and Martín, P. (2024). Update on the role of T cells in cognitive impairment. *Br. J. Pharmacol.* 181, 799–815. <https://doi.org/10.1111/bph.16214>.
87. Lu, T., Ma, L., Xu, Q., and Wang, X. (2022). Blood Th17 cells and IL-17A as candidate biomarkers estimating the progression of cognitive impairment in stroke patients. *J. Clin. Lab. Anal.* 36, e24581. <https://doi.org/10.1002/jcla.24581>.
88. Yu, S., Cui, W., Han, J., Chen, J., and Tao, W. (2022). Longitudinal change of Th1, Th2, and Th17 cells and their relationship between cognitive impairment, stroke recurrence, and mortality among acute ischemic stroke patients. *J. Clin. Lab. Anal.* 36, e24542. <https://doi.org/10.1002/jcla.24542>.
89. Zhang, Y., and Niu, C. (2022). Relation of CDC42, Th1, Th2, and Th17 cells with cognitive function decline in Alzheimer's disease. *Ann. Clin. Transl. Neurol.* 9, 1428–1436. <https://doi.org/10.1002/acn3.51643>.
90. Schmid, R., Petras, D., Nothias, L.-F., Wang, M., Aron, A.T., Jagels, A., Tsugawa, H., Rainer, J., Garcia-Aloy, M., Dührkop, K., et al. (2021). Ion identity molecular networking for mass spectrometry-based metabolomics in the GNPS environment. *Nat. Commun.* 12, 3832. <https://doi.org/10.1038/s41467-021-23953-9>.
91. El Abiead, Y., Strobel, M., Payne, T., Fahy, E., O'Donovan, C., Subramiam, S., Vizcaino, J.A., Zuffa, S., Xing, S., Mannochio-Russo, H., et al. (2024). Enabling pan-repository reanalysis for big data science of public metabolomics data. *Nat. Commun.* 16, 1–7.
92. Bittremieux, W., Avalon, N.E., Thomas, S.P., Kakhkhorov, S.A., Aksenov, A.A., Gomes, P.W.P., Aceves, C.M., Caraballo-Rodríguez, A.M., Gauglitz, J.M., Gerwick, W.H., et al. (2023). Open access repository-scale propagated nearest neighbor suspect spectral library for untargeted metabolomics. *Nat. Commun.* 14, 8488. <https://doi.org/10.1038/s41467-023-44035-y>.
93. Frank, A.M., Monroe, M.E., Shah, A.R., Carver, J.J., Bandeira, N., Moore, R.J., Anderson, G.A., Smith, R.D., and Pevzner, P.A. (2011). Spectral archives: extending spectral libraries to analyze both identified and unidentified spectra. *Nat. Methods* 8, 587–591. <https://doi.org/10.1038/nmeth.1609>.
94. Gauglitz, J.M., West, K.A., Bittremieux, W., Williams, C.L., Weldon, K.C., Panitchpakdi, M., Di Ottavio, F., Aceves, C.M., Brown, E., Sikora, N.C., et al. (2022). Enhancing untargeted metabolomics using metadata-based source annotation. *Nat. Biotechnol.* 40, 1774–1779. <https://doi.org/10.1038/s41587-022-01368-1>.
95. Conway, J.R., Lex, A., and Gehlenborg, N. (2017). UpSetR: an R package for the visualization of intersecting sets and their properties. *Bioinformatics* 33, 2938–2940. <https://doi.org/10.1093/bioinformatics/btx364>.
96. Schmid, R., Heuckeroth, S., Korf, A., Smirnov, A., Myers, O., Dyrland, T. S., Bushuiev, R., Murray, K.J., Hoffmann, N., Lu, M., et al. (2023). Integrative analysis of multimodal mass spectrometry data in MZmine 3. *Nat. Biotechnol.* 41, 447–449. <https://doi.org/10.1038/s41587-023-01690-2>.
97. Nothias, L.-F., Petras, D., Schmid, R., Dührkop, K., Rainer, J., Sarvepalli, A., Protsyuk, I., Ernst, M., Tsugawa, H., Fleischauer, M., et al. (2020). Feature-based molecular networking in the GNPS analysis environment. *Nat. Methods* 17, 905–908. <https://doi.org/10.1038/s41592-020-0933-6>.
98. Kessner, D., Chambers, M., Burke, R., Agus, D., and Mallick, P. (2008). ProteoWizard: open source software for rapid proteomics tools development. *Bioinformatics* 24, 2534–2536. <https://doi.org/10.1093/bioinformatics/btn323>.
99. Heaton, R.K., Franklin, D.R., Ellis, R.J., McCutchan, J.A., Letendre, S.L., Leblanc, S., Corkran, S.H., Duarte, N.A., Clifford, D.B., Woods, S.P., et al. (2011). HIV-associated neurocognitive disorders before and during the era of combination antiretroviral therapy: differences in rates, nature, and predictors. *J. Neurovirol.* 17, 3–16. <https://doi.org/10.1007/s13365-010-0006-1>.
100. Woods, S.P., Rippeth, J.D., Frol, A.B., Levy, J.K., Ryan, E., Soukup, V.M., Hinkin, C.H., Lazzaretto, D., Cherner, M., Marcotte, T.D., et al. (2004). Interrater reliability of clinical ratings and neurocognitive diagnoses in HIV. *J. Clin. Exp. Neuropsychol.* 26, 759–778. <https://doi.org/10.1080/13803390490509565>.
101. Antinori, A., Arendt, G., Becker, J.T., Brew, B.J., Byrd, D.A., Cherner, M., Clifford, D.B., Cinque, P., Epstein, L.G., Goodkin, K., et al. (2007). Updated research nosology for HIV-associated neurocognitive disorders. *Neurology* 69, 1789–1799. <https://doi.org/10.1212/01.WNL.0000287431.88658.8b>.
102. Brennan, C., Belda-Ferre, P., Zuffa, S., Charron-Lamoureux, V., Mohanty, I., Ackermann, G., Allaband, C., Ambre, M., Boyer, T., Bryant, M., et al. (2024). Clearing the plate: a strategic approach to mitigate well-to-well contamination in large-scale microbiome studies. *mSystems* 9, e0098524. <https://doi.org/10.1128/mSystems.00985-24>.
103. Shannon, P., Markiel, A., Ozier, O., Baliga, N.S., Wang, J.T., Ramage, D., Amin, N., Schwikowski, B., and Ideker, T. (2003). Cytoscape: a software

- p>environment for integrated models of biomolecular interaction networks.
- Genome Res.*
- 13, 2498–2504.
- <https://doi.org/10.1101/gr.1239303>
- .
104. Sanders, J.G., Nurk, S., Salido, R.A., Minich, J., Xu, Z.Z., Zhu, Q., Martino, C., Fedarko, M., Arthur, T.D., Chen, F., et al. (2019). Optimizing sequencing protocols for leaderboard metagenomics by combining long and short reads. *Genome Biol.* 20, 226. <https://doi.org/10.1186/s13059-019-1834-9>.
 105. Brennan, C., Salido, R.A., Belda-Ferre, P., Bryant, M., Cowart, C., Tiu, M. D., González, A., McDonald, D., Tribelhorn, C., Zarrinpar, A., et al. (2023). Maximizing the potential of high-throughput next-generation sequencing through precise normalization based on read count distribution. *mSystems* 8, e0000623. <https://doi.org/10.1128/msystems.00006-23>.
 106. Armstrong, G., Martino, C., Morris, J., Khaleghi, B., Kang, J., DeReus, J., Zhu, Q., Roush, D., McDonald, D., Gonazlez, A., et al. (2022). Swapping metagenomics preprocessing pipeline components offers speed and sensitivity increases. *mSystems* 7, e0137821. <https://doi.org/10.1128/msystems.01378-21>.
 107. Zhu, Q., Mai, U., Pfeiffer, W., Janssen, S., Asnicar, F., Sanders, J.G., Belda-Ferre, P., Al-Ghalith, G.A., Kopylova, E., McDonald, D., et al. (2019). Phylogenomics of 10,575 genomes reveals evolutionary proximity between domains Bacteria and Archaea. *Nat. Commun.* 10, 5477. <https://doi.org/10.1038/s41467-019-13443-4>.
 108. Langmead, B., and Salzberg, S.L. (2012). Fast gapped-read alignment with Bowtie 2. *Nat. Methods* 9, 357–359. <https://doi.org/10.1038/nmeth.1923>.
 109. Zhu, Q., Huang, S., Gonzalez, A., McGrath, I., McDonald, D., Haiminen, N., Armstrong, G., Vázquez-Baeza, Y., Yu, J., Kuczynski, J., et al. (2022). Phylogeny-aware analysis of metagenome community ecology based on matched reference genomes while bypassing taxonomy. *mSystems* 7, e0016722. <https://doi.org/10.1128/msystems.00167-22>.
 110. Sepich-Poore, G.D., McDonald, D., Kopylova, E., Guccione, C., Zhu, Q., Austin, G., Carpenter, C., Fraraccio, S., Wandro, S., Kosciolk, T., et al. (2024). Robustness of cancer microbiome signals over a broad range of methodological variation. *Oncogene* 43, 1127–1148. <https://doi.org/10.1038/s41388-024-02974-w>.
 111. Chen, S., Zhou, Y., Chen, Y., and Gu, J. (2018). fastp: an ultra-fast all-in-one FASTQ preprocessor. *Bioinformatics* 34, i884–i890. <https://doi.org/10.1093/bioinformatics/bty560>.
 112. Liao, W.-W., Asri, M., Ebler, J., Doerr, D., Haukness, M., Hickey, G., Lu, S., Lucas, J.K., Monlong, J., Abel, H.J., et al. (2023). A draft human pan-genome reference. *Nature* 617, 312–324. <https://doi.org/10.1038/s41586-023-05896-x>.
 113. Rhie, A., Nurk, S., Cechova, M., Hoyt, S.J., Taylor, D.J., Altemose, N., Hook, P.W., Koren, S., Rautiainen, M., Alexandrov, I.A., et al. (2023). The complete sequence of a human Y chromosome. *Nature* 621, 344–354. <https://doi.org/10.1038/s41586-023-06457-y>.
 114. Schneider, V.A., Graves-Lindsay, T., Howe, K., Bouk, N., Chen, H.-C., Kitts, P.A., Murphy, T.D., Pruitt, K.D., Thibaud-Nissen, F., Albracht, D., et al. (2017). Evaluation of GRCh38 and de novo haploid genome assemblies demonstrates the enduring quality of the reference assembly. *Genome Res.* 27, 849–864. <https://doi.org/10.1101/gr.213611.116>.
 115. Li, H. (2021). New strategies to improve minimap2 alignment accuracy. *Bioinformatics* 37, 4572–4574. <https://doi.org/10.1093/bioinformatics/btab705>.
 116. Danecek, P., Bonfield, J.K., Liddle, J., Marshall, J., Ohan, V., Pollard, M. O., Whitwham, A., Keane, T., McCarthy, S.A., Davies, R.M., et al. (2021). Twelve years of SAMtools and BCFtools. *GigaScience* 10, giab008. <https://doi.org/10.1093/gigascience/giab008>.
 117. Edwards, J.A., and Edwards, R.A. (2019) Fastq-pair: efficient synchronization of paired-end fastq files. <https://doi.org/10.1101/552885>.
 118. Tange, O. (2018). Gnu Parallel. Zenodo. <http://www.doi.org/10.5281/zenodo.1146014>.
 119. Köster, J. (2016). Rust-Bio: a fast and safe bioinformatics library. *Bioinformatics* 32, 444–446. <https://doi.org/10.1093/bioinformatics/btv573>.
 120. Gonzalez, A., Navas-Molina, J.A., Kosciolk, T., McDonald, D., Vázquez-Baeza, Y., Ackermann, G., DeReus, J., Janssen, S., Swafford, A.D., Orchanian, S.B., et al. (2018). Qiita: rapid, web-enabled microbiome meta-analysis. *Nat. Methods* 15, 796–798. <https://doi.org/10.1038/s41592-018-0141-9>.
 121. Hakim, D., Wandro, S., Zengler, K., Zaramela, L.S., Nowinski, B., Swafford, A., Zhu, Q., Song, S.J., Gonzalez, A., McDonald, D., et al. (2022). Zebra: Static and dynamic genome cover thresholds with overlapping references. *mSystems* 7, e0075822. <https://doi.org/10.1128/msystems.00758-22>.
 122. Bolyen, E., Rideout, J.R., Dillon, M.R., Bokulich, N.A., Abnet, C.C., Al-Ghalith, G.A., Alexander, H., Alm, E.J., Arumugam, M., Asnicar, F., et al. (2019). Reproducible, interactive, scalable and extensible microbiome data science using QIIME 2. *Nat. Biotechnol.* 37, 852–857. <https://doi.org/10.1038/s41587-019-0209-9>.
 123. Vázquez-Baeza, Y., Pirrung, M., Gonzalez, A., and Knight, R. (2013). EMPERor: a tool for visualizing high-throughput microbial community data. *GigaScience* 2, 16. <https://doi.org/10.1186/2047-217X-2-16>.
 124. Quality Risk Management Geneva (2005). International Conference on Harmonization (ICH) of Technical Requirements for Registration of Pharmaceuticals for Human Use. Preprint at Topic Q9. https://database.ich.org/sites/default/files/Q9_Guideline.pdf.
 125. Adams, K.J., Pratt, B., Bose, N., Dubois, L.G., St John-Williams, L., Perrott, K.M., Ky, K., Kapahi, P., Sharma, V., MacCoss, M.J., et al. (2020). Skyline for Small Molecules: A Unifying Software Package for Quantitative Metabolomics. *J. Proteome Res.* 19, 1447–1458. <https://doi.org/10.1021/acs.jproteome.9b00640>.
 126. Melnik, A.V., da Silva, R.R., Hyde, E.R., Aksenov, A.A., Vargas, F., Bouslimani, A., Protsyuk, I., Jarmusch, A.K., Tripathi, A., Alexandrov, T., et al. (2017). Coupling targeted and untargeted mass spectrometry for metabolome-microbiome-wide association studies of human fecal samples. *Anal. Chem.* 89, 7549–7559. <https://doi.org/10.1021/acs.analchem.7b01381>.
 127. Bittremieux, W., Chen, C., Dorrestein, P.C., Schymanski, E.L., Schulze, T., Neumann, S., Meier, R., Rogers, S., and Wang, M. (2020). Universal MS/MS Visualization and Retrieval with the Metabolomics Spectrum Resolver Web Service. Preprint at bioRxiv, 2020.05.09.086066. <https://doi.org/10.1101/2020.05.09.086066>.

STAR★METHODS

KEY RESOURCES TABLE

REAGENT or RESOURCE	SOURCE	IDENTIFIER
Antibodies		
LIVE/DEAD™ Fixable Yellow Dead Cell Stain Kit	Life Technologies	L34968
CD4 Monoclonal Antibody (clone RM4-5), APC-eFluor™ 780	eBioscience	Cat# 47-0042-82; Lot# 2431517
Foxp3 Monoclonal Antibody (clone: FJK-16s), FITC	eBioscience	Cat# 11-5773-82; Lot #2984316
Roryt Mouse Anti Mouse (clone: Q31 378), Brilliant Violet 421	BD Biosciences	Cat# 562894; Lot# 4093064
Tbet Monoclonal Antibody (clone: 4B10), PE/Dazzle 594	Biolegend	Cat# 644828; Lot# B402685
Biological samples		
Human fecal samples	HIV Neurobehavioral Research Center (HNRC)	UCSD Human Research Protections Program, HNRC IRB#172092
Chemicals, peptides, and recombinant proteins		
Histamine-C2:0	Sigma-Aldrich	673-49-4
Histamine-C3:0	EnamineStore	37622-30-3
Histamine-C4:0	EnamineStore	710311-88-9
Histamine-C5:0	EnamineStore	1007671-42-2
Histamine-C6:0	Aldlab Chemicals	103827-10-7
Cadaverine-C2:0	Sigma-Aldrich	32343-73-0
Cadaverine-C3:0	EnamineStore	65251-14-1
Cadaverine-C5:0	Aldlab Chemicals	1341377-80-7
Cadaverine-C6:0	Aldlab Chemicals	1338959-33-3
Cadaverine-C7:0	Aldlab Chemicals	1593857-16-9
Dopamine-C2:0	Sigma-Aldrich	2494-12-4
Serotonin-C2:0	Sigma-Aldrich	1210-83-9
Tryptophan-C3:0	Aldlab Chemicals	79198-76-8
Recombinant Mouse GM-CSF (carrier-free)	Biolegend	Cat# 576308
Recombinant Murine IL-2	Peptotech	Cat# 212-12-20UG
Anti-mouse CD3e Functional Grade Purified	eBioscience	Cat# 16-0031-86
Mouse IL-23 Recombinant Protein	eBioscience	Cat# 14-8231-63
Recombinant Murine IL-6	Peptotech	Cat# 216-16
Recombinant Murine IL-1β	Peptotech	Cat# 211-11B
Critical commercial assays		
Naive CD4 ⁺ T Cell Isolation Kit	Miltenyi Biotec	Cat# 130-104-453
Deposited data		
N-acyl lipids library	This paper	https://doi.org/10.5281/zenodo.14015198
Untargeted LC-MS/MS data of mice - feces (diet and antibiotics treatment)	Michael Karin	GNPS/MassIVE: MSV000080918
Untargeted LC-MS/MS data from the body decomposition study - skin swabs and soil	Jessica L. Metcalf	GNPS/MassIVE: MSV000084322; MSV000084463
Untargeted LC-MS/MS data from the diabetes study - urine	Jane J. Kim	GNPS/MassIVE: MSV000082261
Untargeted LC-MS/MS data from the monocolonized germ-free mice study - small intestine and colon	Dennis Kasper	GNPS/MassIVE: MSV000088040
Untargeted LC-MS/MS data from the HIV study	HIV Neurobehavioral Research Center (HNRC)	GNPS/MassIVE: MSV000092833
Untargeted LC-MS/MS data of the microbial monocultures	This paper	GNPS/MassIVE: MSV000095648
NMR of N-acyl lipids	This paper	https://doi.org/10.5281/zenodo.14015081

(Continued on next page)

Continued

REAGENT or RESOURCE	SOURCE	IDENTIFIER
<i>N</i> -acyl lipids retention time and MS/MS matching	This paper	GNPS/MassIVE: MSV000095423
<i>N</i> -acyl lipids quantification and method validation	This paper	GNPS/MassIVE: MSV000096049
Experimental models: Organisms/strains		
Wild-type C57BL/6J mice	The Jackson Laboratory	Strain# 000664; RRID:IMSR_JAX:000664
Software and algorithms		
MassQL	Jarmusch et al. ¹	https://massql.gnps2.org/
fastMASST	Robin Schmid, https://fasst.gnps2.org/fastsearch/	https://github.com/robinschmid/microbe_masst
microbeMASST	Zuffa et al. ¹⁸	https://masst.gnps2.org/microbemasst/
plantMASST	Gomes et al. ²⁰	https://masst.gnps2.org/plantmasst/
foodMASST	West et al. ¹⁹	https://masst.gnps2.org/foodmasst2/
ReDU	Jarmusch et al. ² ; Abiead et al. ⁹¹	https://redu.gnps2.org/
Mmvec	Morton et al. ⁴¹	https://github.com/biocore/mmvec

EXPERIMENTAL MODEL AND STUDY PARTICIPANT DETAILS**Bacterial culture conditions**

A list of all the 78 bacteria used in this study are listed in the Table S2. All bacteria cultures were started from glycerol stock and incubated at 37°C anaerobically (10% CO₂, 7.5% H₂, 82.5% N₂) in a filtered Brain Heart Infusion (BHI) medium (Table S2) at a pH adjusted to 7.2 using 5 N NaOH.

Human fecal material

All procedures involving human participants adhered to the ethical standards established by the institutional and/or national research committee (UCSD Human Research Protections Program, HNRC IRB#172092). Briefly, participants were 56.3± 11.5 years old, with 74.5% male, and 69.9% were diagnosed with HIV. The cohort included 40.4% Hispanic, 44.4% non-Hispanic White, and 15.1% Black individuals. More details on the participants are available in the Table S3. All participants signed a consent to all study procedures.

METHOD DETAILS**Searches in LIPID MAPS**

An initial search in LIPID MAPS¹² was performed searching for any compound in the database that would have an amide bound, which resulted in 5,648 substructures. Ceramides were filtered out, resulting in a total of 1,240 compounds that comprised a mixture of fatty acid-derived *N*-acyl lipids, bile acid amidates, lipids attached to CoA, and *N*-acylated molecules, such as deferioxamine and other natural products. These compounds were that were manually inspected to determine if these were *N*-acyl lipids (Table S1). The headgroups and acyl chain lengths were plotted (Figures S1A and S1B) using the "seaborn.barplot" package (version 0.12.2) in Python (version 3.7.6).

Design of the MassQL queries and creation of the *N*-acyl lipids library

N-acyl lipids were searched in the GNPS/MassIVE public datasets, which consist of ~1.2 billion spectra, and 2,706 datasets when this search was performed in 2023. This search was initially conducted with Orbitrap public data deposited in the GNPS/MassIVE repository using the Mass Spec Query Language (MassQL).¹ MassQL enables the filtering of public mass spectrometry data to retrieve all MS/MS spectra that contain defined and recognizable data patterns, and can also be done at the repository level. Since *N*-acyl lipids ionize well in positive ionization mode and more than 90% of the public mass spectrometry data was acquired in this mode, only positive ionization data was mined from the public domain.

The queries were developed for biologically relevant molecules conjugated to an acyl lipid chain via an amide bond (Figure 1A). The headgroups contained a primary or secondary amine. In total, queries were designed for 64 heads, including proteinogenic amino acids, polyamines, endocrine hormones, neurotransmitters, and other selected diagnostic-relevant metabolites, ranging from serotonin to kynurenine, and from thyroxine (T4) to glutathione (see Table S1 for the complete list of molecules for which a query was developed). We directed our searches to compounds in which the acyl chain varies from two up to 30 carbons, and from zero up to four unsaturations. In addition, no attachments to the acyl chain (such as hydroxylations) were considered. The queries were designed by manually inspecting reference MS/MS spectra of compounds previously synthesized,¹⁶ and we observed that in the vast majority of the cases, the acylium ion—resulting from the stable fatty acid chain fragmentation—was generally absent or present at

very low abundances (see Figure S1C). Consequently, each query was designed to target key MS/MS fragments of the headgroup, in addition to the 129 theoretical precursor ions for each potential *N*-acyl lipid considering the precursor ions as protonated molecules ($[M+H]^+$) (Figure S1D). For the compounds for which there were no reference MS/MS libraries, the fragmentation pattern of the heads alone was manually inspected and these patterns were used in addition to the precursor ion inclusion list for each head. A simplified example of a query designed for phenylalanine as a headgroup (Figures S1C and S1D) is shown below.

```
QUERY scaninfo(MS2DATA) WHERE MS2PREC=(208.0968 OR 222.1124 OR ... OR 578.4596 OR 592.4752):TOLERANCEPPM=20
AND MS2PROD=166.0863:TOLERANCEPPM=20 AND MS2PROD=120.0808:TOLERANCEPPM=20:INTENSITYPERCENT=50
```

Once the candidate queries were formulated, their selectivity was initially evaluated by conducting the queries in the GNPS public spectral libraries which contained 587,917 spectra of a wide variety of classes of compounds. All job links are available in Table S1). A false discovery rate (FDR) was estimated by checking the retrieved spectra for each query that matched. We assessed this manually by examining the structures of the spectral matches and determining if they made sense with respect to the expected fragmentation. In cases such as alanine versus sarcosine, which are isomers and have very similar MS/MS spectra, both were accepted as true positives. Matches where the headgroup aligned with the expected fragmentation pattern were considered positive matches, while anything that did not match the headgroup was considered a false positive. Some matches were relative to putative spectra created through the propagation of a molecular network and could match related molecules but be derived from different headgroups (Table S1).⁹² Therefore, hits against suspect spectra were not considered. If a high FDR was obtained for the GNPS library searches, the query was iteratively refined until the lowest possible FDR was obtained.

The final queries were then run against publicly available Orbitrap data in GNPS/MassIVE between July and October 2023 (Table S1). As an additional performance assessment, but now of the repository-scale query results, all of the MS/MS spectra derived from each MassQL query were searched against all publicly available reference spectra in GNPS. The parameters used for the searches were as follows: cosine threshold as above 0.7, minimum matched fragments as 6, and precursor and fragment ion mass tolerance set to 0.02 Da. For almost all queries, the mismatched spectra comprised less than 1% of the spectral matches, except for glycine (FDR 1.5%), which had false positives to ethanolamine conjugates. Some other queries showed an FDR greater than 1%, but these false positives were matches to suspect spectra (Table S1).⁹²

The queries resulted in the retrieval of a total of 176,732 MS/MS spectra from Orbitrap data in the public domain (Figure S1E). Six headgroups—selenomethionine, 3-methoxytyrosine, 3-iodothyronamine, levothyroxine (T4), liothyronine (T3), and homocysteine/homocystine—had no candidate *N*-acyl lipid MS/MS matches retrieved. Identical MS/MS spectra obtained from the MassQL queries were merged using MScluster⁹³ to reduce duplications, keeping also only the ones that were retrieved at least twice (all GNPS job links are available in Table S1). This step resulted in 1,474 unique candidate *N*-acyl lipids (Figure S1E).

Because some headgroups would result in very few diagnostic ions (e.g., glycine) and could result in spurious matches, an additional filtering step was applied in these results to increase the confidence of the library. This filter was based on cosine similarity calculation between the MS/MS spectra retrieved from the queries and the reference spectra of the compounds previously synthesized.¹⁶ In cases where there were no reference MS/MS spectra available, a modified cosine similarity calculation was performed between the MS/MS retrieved from the query and the reference MS/MS of the headgroup. Therefore, spectra would only pass the filter if the cosine or modified cosine similarity scores would reach values above 0.7. The resulting list of MassQL-filtered spectra represented 851 unique candidate *N*-acyl amides (Table S1, Figure S1E), which were used to generate an MS/MS spectral library and leveraged for downstream analyses. This library, named GNPS-N-ACYL-LIPIDS-MASSQL, is currently part of the public GNPS spectral libraries and can be browsed on the web interface at the following link: <https://gnps.ucsd.edu/ProteoSAFe/gnpslibrary.jsp?library=GNPS-N-ACYL-LIPIDS-MASSQL>.

***N*-acyl lipids repository-scale search**

To expand our investigations beyond Orbitrap datasets, we conducted a repository-scale search using a fast MASST (FASST) search,³⁰ an updated and faster version of the Mass Spectrometry Search Tool (MASST),²¹ against all the public domain data that were indexed in GNPS.²² This search is based on the cosine similarity of the queried spectra against the ones from the public domain in GNPS/MassIVE, regardless of the instrument used for data acquisition. The MGF files generated with MScluster were used as input in the FASST search pipeline, and the parameters used for this search were: cosine similarity above 0.7, minimum matched fragments as 4, and precursor ion and fragment ion tolerances as 0.02 Da. These searches were conducted using the REST web API (<https://zenodo.org/records/7828220>) in October 2023, using *gnps_index*. In addition to getting a table with all the MS/MS spectra matches from the public datasets, outputs from domain-specific MASSTs are also generated with this search: (1) *microbeMASST*: merges the FASST spectral matches against a curated database of more than 60,000 LC-MS/MS files of microbial monocultures that were taxonomically defined¹⁸; (2) *plantMASST*: merges the FASST matches against 19,075 LC-MS/MS files of plant extracts of taxonomically defined plants²⁰; and (3) *foodMASST*: merges FASST matches against ~3,500 LC-MS/MS files of foods and beverages categorized within a food ontology, collected as part of the Global FoodOmics project.^{19,94} These domain-specific MASSTs generated output tables that contain spectral matches to specific data files in the public domain that can be mapped to the curated list of taxonomy/ontology-defined metadata. Therefore, it is possible to map in which microbes, plants, or foods a particular *N*-acyl lipid was previously acquired and deposited in GNPS/MassIVE.

The FASST search enabled us to retrieve 356,542 MS/MS spectra from 61,833 files in 950 datasets and emphasizes how common *N*-acyl lipids are detected in untargeted metabolomics experiments (Table S1). To explore their distribution in different organisms, tissues, and biofluids, we merged the FASST output with the ReDU (Reanalysis of Data User Interface) controlled vocabulary meta-data, which enables us to do comparisons across datasets.² This merged table was filtered to contain only rows relative to human ("9606|Homo sapiens") or rodent-related datasets ("10088|Mus", "10090|Mus musculus", "10105|Mus minutoides", "10114|Rattus", "10116|Rattus norvegicus") in the NCBITaxonomy column. Therefore, the total number of unique MS/MS spectra obtained for humans, rodents, microbes, plants, and foods was 39,525, 28,497, 29,105, 3,754, and 6,537, respectively (Figure S1E).

The FASST searches are performed on indexed spectra, which are MS/MS spectra that are filtered to allow the repository searches to be conducted in seconds. To increase the level of confidence of these matches, an additional cosine similarity was performed on the FASST results to calculate the cosine similarity between the queried spectra and the pre-indexed unfiltered spectra. We filtered these results by removing any MS/MS that resulted in a cosine below 0.7 (Figure S1E). Therefore, the final numbers based on ReDU and domain-specific MASST analysis were the following: 31,299 of the MS/MS spectra could be linked to human samples, 21,866 were found in rodent-related datasets, 22,589 found in microbial monocultures, 2,931 in plant-related data, and 5,576 MS/MS in foods (Figure S1E).

The *N*-acyl lipids results obtained from the microbeMASST results were further filtered to: (1) remove any *N*-acyl lipid that was observed in human cell lines (which are also included in microbeMASST as control of host-derived compounds) by filtering outputs in which the taxaname was "Homo sapiens"; (2) remove *N*-acyl lipids that were retrieved only one or two times in the microbeMASST searches; and (3) remove *N*-acyl lipids that appear more than 5% in blanks or QCs (also added in microbeMASST). For the *N*-acyl lipids results of plantMASST, filters (2) and (3) were applied in a similar way. For the foodMASST results, filter (2) only was applied as there are no blanks or QC samples part of foodMASST.

The polarity indexes of the solvent mixtures used to obtain the extracts relative to the files retrieved in our MASST searches were calculated based on the Snyder indexes. More specifically, the column 'SampleExtractionMethod' from the ReDU table was inspected, and the estimation was calculated through the following weighted formula:

$$P' = \frac{\sum(P_i \times R_i)}{\sum(R_i)}$$

Where:

P_i = polarity index of solvent i

R_i = ratio of solvent i in the mixture

The results of the queries (Figure 1C), body part distributions (Figures 1D, 1E, S2C, and S2D), and microbeMASST (Figures 2A and 2B) are shown in the form of heatmaps that were created using the "seaborn.clustermap" package (version 0.12.2) in Python (version 3.7.6). The microbial classes were organized in taxonomic order according to NCBI Taxonomy ID. The UpSet plots (Figures 2C and S3A–S3D) were generated in R (<https://www.R-project.org/>, version 4.0.0) using the "UpSetR" package (version 1.4.0).⁹⁵ Barplots (Figures 2B and 2D) were created using the "seaborn.barplot" package (version 0.12.2) in Python (version 3.7.6). Venn diagrams (Figure S2C) were created using the matplotlib_venn library in Python (version 3.7.6.)

Reanalysis of public data from GNPS/MassIVE

The *N*-acyl lipids library created was used to reanalyze several public datasets available in GNPS/MassIVE: (1) a study on mono-colonized germ-free mice (MSV000088040, small intestine and colon samples); (2) a type-1 diabetes study (MSV000082261, urine samples); (3) a study on body decomposition (MSV000084322 and MSV000084463, skin and soil samples); and (4) a dataset on the effect of diet and antibiotics consumption in colorectal cancer (MSV000080918, fecal samples). For each dataset, the files were downloaded from GNPS/MassIVE and processed in MZmine3 (version 3.9.0).⁹⁶ The parameters used for each study are available in Table S2, and the MZmine3 batch files are available at https://github.com/helenamrusso/N-acyl_lipids. The output files generated at the processing step (.csv file with peak areas and .mgf files with MS/MS information of each feature) were used as inputs in the Feature-Based Molecular Networking⁹⁷ workflow in GNPS2 and was against the *N*-acyl lipids library.²² The parameters of this workflow were the same for all the datasets, in which the precursor and fragment ions tolerances were set to 0.02 Da, the minimum matching peak between the queried spectra and the library was set to 4, a cosine threshold of 0.7 was applied, and no filters considered. The GNPS2 FBMN jobs can be accessed at:

Monocolonized germ-free mice dataset (MSV000088040): <https://gnps2.org/status?task=55122ffb51ab4957be51b0073abc8f04>

Diabetes dataset (MSV000082261): <https://gnps2.org/status?task=ed2d2cd94179481d818356271bd7762f>

Body decomposition datasets (MSV000084322 and MSV000084463): <https://gnps2.org/status?task=5f30dc8527bb456190daf2e772bf399d>

Impact of diet and antibiotics consumption in colorectal cancer dataset (MSV000080918): <https://gnps2.org/status?task=ba8fd7da3d654d1d949d4beb398b4152>

For the monocolonized germ-free mice, a heatmap was obtained to show the log₂ of the fold change of *N*-acyl lipids levels of colonized and monocolonized mice in relation to the germ-free group (Figure S3F). To achieve this, the median of each feature annotated as an *N*-acyl lipid was calculated and the log₂(FC) was calculated. The small intestine and colon samples were considered separately.

The heatmap was created using the "seaborn.clustermap" package (version 0.12.2) in Python (version 3.7.6). The microbial strains were organized in taxonomic order according to NCBI Taxonomy ID and their classes were also mapped to the heatmap. The *N*-acyl lipids were organized in ascending order in the number of carbons and unsaturations.

To determine if the *N*-acyl lipid matches had a significant correlation with any of the groups in each study, the peak areas (exported. csv file from MZmine3) of the matching compounds in the datasets were plotted as boxplots using the "seaborn.boxplot" package (version 0.12.2) in Python (version 3.7.6).

Line plots were obtained for the body decomposition dataset to show the changes in *N*-acyl lipids with increasing body decomposition levels (Figures S3I and S3J). The mean of each feature annotated as an *N*-acyl lipid was calculated for each stage of decomposition and a line plot was obtained using Matplotlib (version 3.2.1) in Python (version 3.7.6). Finally, volcano plots were obtained for the diet and antibiotics treatment study, where the $\log_2(\text{FC})$ was calculated for each *N*-acyl lipid (Figures 2E and 2F), and scatter plots were obtained with Matplotlib (version 3.2.1) in Python (version 3.7.6).

Bacterial cultures screening

Microbial growth and metabolite extraction

Cultures were normalized at $\text{OD}_{600} = 0.02$ before being diluted 1/10 in 1 mL of mPYG medium (Table S2) and incubated for 48–72 h at 37°C in a 2 mL deep-well plate. Following bacterial growth, 400 μL of culture was transferred to a new 2 mL deep-well plate and extracted overnight at 4°C with 1.2 mL of pre-chilled 50% MeOH/H₂O. Samples were dried in a CentriVap and stored at -80°C until LC-MS/MS analysis.

LC-MS/MS untargeted metabolomics analysis

The microbial extracts were resuspended in 200 μL of 50% MeOH/H₂O with 1 μM of sulfadimethoxine as internal standard, incubated at -20°C overnight before being centrifuged at 21,130 $\times g$. Then, 150 μL was transferred into a 2 mL glass vial containing an insert. The chromatographic separation was performed by reversed-phase polar C18 (Kinetex Polar C18, 100 mm \times 2.1 mm, 2.6 μm , 100 Å pore size with a guard column, Phenomenex) using a Vanquish UHPLC system coupled to a Q-Exactive Orbitrap mass spectrometer (Thermo Fisher Scientific). The mobile phase consisted of solvent A (water + 0.1% formic acid) and solvent B (ACN + 0.1% formic acid) and the column compartment was kept at 40 °C. Five microlitres of the samples were injected and eluted at a flow rate of 0.5 mL/min using the following gradient: 0 – 1.1 min 5% B, 1.1 – 7.5 min 40% B, 7.5 – 8.5 min 99% B, 8.5 – 9.5 min 99% B, 9.5 – 10 min 5% B, 10 – 10.5 min 5% B, 10.5 – 10.75 min 99% B, 10.75 – 11.25 min 99% B, 11.5 – 12 min 5% B. Mass spectrometry (MS) analysis was performed using electrospray ionization (ESI) in positive ionization mode. The parameters were set as follows: Sheath gas flow 53 L/min, auxiliary gas flow rate 14 L/min, sweep gas flow 3 L/min, spray voltage 3.5 kV, inlet capillary to 269°C, and auxiliary gas heater set to 438°C. MS scan range 100 – 1000 m/z with a resolution ($R_{m/z\ 200}$) of 35,000 with 1 microscans. The automatic gain control (AGC) target was set to 1E6 with a maximum injection time of 100 ms. Up to 5 MS/MS spectra per MS1 were collected with a resolution ($R_{m/z\ 200}$) set to 17,500 with 1 microscans, maximum injection time of 150 ms with an AGC target of 5E5. The isolation window was set to 1 m/z and the isolation offset at 0 m/z . The normalized collision energy was acquired with an increase stepwise at 25, 40, and 60. The apex trigger was set to 2 – 15 s and a dynamic exclusion of 5 s. Isotopes were excluded from the analysis. The data is publicly available on GNPS/MassIVE MSV000095648.

Data processing, molecular networking, and data visualization

The LC-MS/MS files were converted to.mzML using MSConvert (ProteoWizard, Palo Alto, CA, USA)⁹⁸ and processed in MZmine4 (version 4.0.8).⁹⁶ The parameters used for data processing are listed in Table S2. The exported files were subjected to the FBMN⁹⁷ workflow in GNPS2.²² The parameters used for the library search for *N*-acyl lipids annotation were as follows: precursor and fragment ion tolerances set to 0.02 Da, 4 minimum matched peaks between the queried spectra and the library, a cosine threshold of 0.7, and no filters considered. The GNPS2 FBMN job can be accessed at <https://gnps2.org/status?task=cff8c1a5895b4b9b917c36ad9444c635>.

A heatmap was obtained to show the variations of the features annotated as *N*-acyl lipids with regard to the microbial media. A median value was obtained for all the media samples, and for all the bacteria. A filter was applied to only consider the features that were detected in both microbial replicates. Therefore, if there were any zero values for one of the microbial replicates, all values were set to zero. The $\log_2(\text{FC})$ was calculated and plotted using the "seaborn.clustermap" package (version 0.12.2) in Python (version 3.7.6). The microbial strains were organized in taxonomic order according to NCBI Taxonomy ID and their classes were also mapped to the heatmap. The *N*-acyl lipids were organized in ascending order in the number of carbons and unsaturations.

Combinatorial reactions of *N*-acyl lipids

Fatty acid (1 eq.) and 2 mL of THF were added to a 20 mL scintillation vial with a magnetic stir bar. To this solution, solid EDC (1 eq.) and neat DIPEA (1 eq.) were subsequently added, and the solution was stirred at RT. After 15 minutes, amine compound (1 eq.) in 1 mL H₂O was added, and the reaction was stirred for 14 h. To proceed with LC-MS/MS analyses, 1 μL of the reaction mixture was diluted in 1 mL of LC-MS grade MeOH.

HIV Neurobehavioral Research Center (HNRC) cohort study

Cohort

HIV RNA levels in plasma were measured from blood samples using a commercial reverse transcriptase-polymerase chain reaction assay (Amplicor version 1.5, Roche Diagnostics, Indianapolis, IN, USA). The levels were log transformed, and participants were categorized as having an undetectable viral load if their HIV RNA levels were less than or equal to 50 copies/mL. The neurocognitive test battery included measures that assess seven neurocognitive domains commonly affected by HIV, including verbal fluency, processing speed, executive functioning, learning, recall, working memory, and motor speed.⁹⁹ Raw scores for each test were converted to demographically corrected T-scores and used to derive global clinical ratings using a published standardized algorithm that classifies the presence and severity of NCI. Global ratings have a nine-point scale ranging from normal (1-4), to mildly impaired (5-6), to moderately or severely impaired (7-9), with a clinical rating of greater than or equal to 5 indicative of NCI.¹⁰⁰ This is consistent with Frascati's Criteria for diagnosing HIV-associated neurocognitive disorder, which requires at least mild neurocognitive impairment in at least two of the seven neurocognitive ability domains.¹⁰¹

Sample preparation

The study was conducted following protocols approved by the UCSD Human Research Protections Program (<https://irb.ucsd.edu/>), and all participants gave written informed consent before participating. Stool samples were processed using a recently developed automated pipeline designed for simultaneous extraction of metagenomic and metabolomic data.¹⁰² For the metabolites extraction, the swabs were placed into Matrix Tubes (ThermoFisher Scientific, MA, USA) containing 400 μ L of 95% ethanol (v/v), and the tubes were sealed using the Capit-All automated capping instrument (ThermoFisher Scientific, MA, USA). The tubes were shaken at 1,200 rpm for 2 min using a SpexMiniG plate shaker, followed by centrifugation at 2,700 g for 5 min. Part of the supernatant (200 μ L) was transferred to a deep well plate with an 8-channel pipette, dried down in a vacuum centrifuge concentrator at room temperature for approximately 5 h, and stored at -80°C until LC-MS/MS analyses.

LC-MS/MS untargeted metabolomics analysis

Prior to the analyses, the samples were resuspended in 200 μ L of acetonitrile:H₂O (1:1, v/v) with 100 μ g/L sulfadimethoxine as the internal standard, sonicated for 10 min, centrifuged at 450 g for 10 min, and 150 μ L of the supernatant was transferred to a shallow 96 well plate for analyses. The extracts were injected (5 μ L) into a Vanquish UHPLC system coupled to a Q-Exactive Orbitrap mass spectrometer (Thermo Fisher Scientific). The chromatographic separation was achieved by reverse-phase polar C18 (150 \times 2.1 mm, 2.6 μ m particle size, 100 Å pore size; Phenomenex, Torrance) with a SecurityGuard C18 column (2.1 mm ID) at 30 °C column temperature. The mobile phase consisted of solvents A (water) and B (ACN) both containing 0.1% formic acid, and the flow rate was set at 0.5 mL/min. The following gradient was applied: 0-1 min 5% B, 1-7 min 5-99% B, 7-8 min 99% B, 8-8.5 min 99-5% B, 8-10 min 5%B. Mass spectrometry (MS) analysis was performed using electrospray ionization (ESI) in positive ionization mode, and the parameters were set as follows: sheath gas flow 53 L/min, auxiliary gas flow rate 14 L/min, sweep gas flow 3 L/min, spray voltage 3.5 kV, inlet capillary to 269°C, and auxiliary gas heater 400 °C. MS1 scan range was set to m/z 100-1500 with a resolution ($R_{m/z\ 200}$) of 35,000, automatic gain control (AGC) target as 5.0E4, and maximum injection time of 100 ms. Up to 5 MS/MS spectra per MS1 were collected with a resolution ($R_{m/z\ 200}$) set to 17,500, AGC target as 5.0E4, and maximum injection time of 100 ms. The isolation window was set to 3 m/z and the isolation offset was set to 0.5 m/z . The normalized collision energy was acquired with an increased stepwise from 20 to 30 to 40%. The apex trigger was set to 2 - 15 s, the minimum AGC target for the MS/MS spectrum was 5.0E3, and a dynamic precursor exclusion of 10 s was selected. This dataset is publicly available in GNPS/MassIVE under the following accession number: MSV000092833

Data processing, Feature-Based Molecular Networking, and probability calculation

The LC-MS/MS files were converted to mzML using MSConvert (ProteoWizard, Palo Alto, CA, USA)⁹⁸ and processed in MZmine3 (version 3.9.0).⁹⁶ The parameters used for data processing are listed in Table S2. The exported files were subjected to the FBMN⁹⁷ workflow in GNPS2.²² No filters were applied to the data, and the precursor and MS/MS fragment ion tolerances were set to 0.02 Da. A molecular network was created, in which the edges were filtered to have a cosine score above 0.7 and at least four matched fragments. Similarly, the parameters for the *N*-acyl lipids library search were set to have a cosine value above 0.7 and at least four matched fragments. The GNPS2 FBMN job can be accessed at <https://gnps2.org/status?task=ee34ee95908749dd81ee9a62fbdac98e>. The molecular networks were visualized in Cytoscape¹⁰³ (version 3.10.0).

A probability of random matches to the *N*-acyl lipids library was estimated by taking into account the following criteria:

Number of *N*-acyl cadaverines in the library = 15

Number of total *N*-acyl lipids in the library = 851

The probability of getting a match to five *N*-acyl cadaverines out of the 15 *N*-acyl cadaverines part of the *N*-acyl lipids resource, compared to the whole pool of 851 *N*-acyl lipids is given by the following equation:

$$P = \frac{\binom{15}{5}}{\binom{851}{5}}$$

$$P = 3003 / 3,675,819,629,020 = 8.17 \times 10^{-10}$$

Metagenomic data sequencing

Fecal samples were processed for shotgun metagenomics sequencing as previously described.¹⁰⁴ The metagenomic libraries were normalized by iSeq (Illumina) read count distribution to generate a final pool that made sequencing on the NovaSeq more efficient.¹⁰⁵ Raw sequence files were demultiplexed using BaseSpace (Illumina, CA, USA), and quality-filtered following a previous protocol.¹⁰⁶ The filtered reads were aligned to the Web of Life database¹⁰⁷ using bowtie2,¹⁰⁸ and the settings used were the following: maximum and minimum mismatch penalties (mp=[1, 1]), a penalty for ambiguities (np=1; default), read and reference gap open- and extend penalties (rdg=[0, 1], rfg=[0, 1]), a minimum alignment score for an alignment to be considered valid (score-min=[L, 0, -0.05]), a defined number of distinct, valid alignments (k=16), and the suppression of SAM records for unaligned reads, as well as SAM headers (no-unal, no-hd). A feature table was obtained by converting the resulting alignments using the Web of Life Toolkit App.¹⁰⁹

Metagenomic data processing

The metagenomic data processing was performed as previously described.¹¹⁰ The sequence data were filtered for all adapters known to fastp (version 0.23.4) in paired-end mode by explicitly specifying a known adapters file.¹¹¹ Fastp also removed sequences shorter than 45 nucleotides with -l, a flag to filter the minimum length of each sequence. Each sample was then filtered against each genome in the human pangenome,¹¹² as well as both T2T-CHM13v2.0¹¹³ and GRCh38,¹¹⁴ using minimap2¹¹⁵ (version 2.26-r1175) with “-ax sr” for short read mode. The data were first run in paired-end mode, and then run in single-end mode, per genome. Each successive run was converted from SAM to FASTQ using samtools¹¹⁶ (version 1.17) with arguments -f 12 -F 256 -N for paired-end data and -f 4 -F 256 for single-end. The single-end data are repaired using fastq_pair¹¹⁷ (version 1.0) specifying a table size of 50M with -t. Compute support was provided with GNU Parallel¹¹⁸ (version 20180222). Single-end FASTQ output from samtools was split into R1 and R2 with a custom Rust program, with rust-bio for parsing¹¹⁹ (version 1.4.0). Data were multiplexed with sed and demultiplexed using a custom Python script. Shotgun sequencing data were then uploaded to and processed through Qiita¹²⁰ (Study ID 11135). Sequence adapter and host filtering were executed using qp-fastp-minimap2 version 2022.04. Subsequently, Woltka¹⁰⁹ version 0.1.4 (qp-woltka 2022.09) with the Web of Life 2 database was employed for taxonomic and functional predictions. Genomic coverages were computed, and features with less than 25% coverage were excluded.¹²¹ To further enhance data quality, a prevalence filter using QIIME 2 v2023.5¹²² was applied, eliminating features present in less than 10% of samples to mitigate the inclusion of erroneous and low-quality reads. The resulting feature table was utilized for downstream analysis.

Microbe-metabolite multi-omics associations

Co-occurrence probabilities between microbes and metabolites were calculated using mmvec⁴¹ (version 1.0.4) as a Qiime2¹²² plugin. Mmvec takes as input the relative abundance matrix for the sequencing data and the feature abundance table for the ion features, and through a neural networking approach, conditional probabilities of observing molecules based on the abundance of each microbe are calculated. A subset of samples with both metabolite and microbiome data were used for this analysis (225 samples). The mmvec parameters were as follows: -p-batch-size 50, -p-num-testing-examples 5, -p-epochs 50, -p-learning-rate 1e-4. All other parameters for the analyses were set as the default values. EMPor¹²³ was used to visually inspect the feature-feature biplots (<https://view.qiime2.org/>). The spheres on the plot were colored based on which group (HIV+ vs HIV-) the molecules were most abundant, and the arrows indicate the 30 most important OTUs retrieved from the analyses (i.e., higher magnitude of the vector using Euclidean distance from the origin) (Figure 3D). The co-occurrence probabilities were also inspected at the microbial order taxonomic level for the histamine and cadaverine *N*-acyl lipids. Only histamine-C2:0 and histamine-C3:0 had co-occurrence probabilities > 6.0, and a network was obtained for the microbial orders that were shared between both compounds (Figure 3E). The network was visualized in Cytoscape¹⁰³ (version 3.10.0). All inputs and outputs from mmvec and the Cytoscape visualization file are available at https://github.com/helenamrusso/N-acyl_lipids.

Microbial cultures from the multi-omics analysis

Holdemanella biformis DSM 3989, *Catenibacterium mitsuokai* DSM 15897, *Megasphaera* sp. DSMZ 102144, *Dorea longicatena* DSM 13814, *Prevotella buccae* D17, *Eubacterium siraeum* DSM 15702, *Collinsella aerofaciens* ATCC 25986, *Roseburia inulinivorans* DSM 16841, and *Streptococcus thermophilus* LMD-9 were selected for microbial culturing based on the multi-omics results and strains availability. These microbes were cultured in 200 μ L in BHI medium (Table S2) for 72 h at 37°C in an anaerobic chamber supplemented with 100 μ M of cadaverine, putrescine, and histamine. Samples were extracted overnight at 4°C using 600 μ L of pre-chilled 50% MeOH/H₂O. Samples were then dried using a CentriVap and stored at -80°C until resuspension.

Untargeted LC-MS/MS analysis of microbes from the multi-omics HIV analysis

The microbial extracts were resuspended in H₂O (100%) containing 1 μ M of sulfamethazine to achieve a concentration of 50 mg/mL, incubated at -20°C overnight, and centrifuged at 21,130 \times g. Then, 120 μ L of the solution was transferred to a 2 mL glass vial containing an insert for LC-MS/MS analysis. The samples were injected (2 μ L) into a Vanquish UHPLC system coupled to a Q-Exactive Orbitrap mass spectrometer (Thermo Fisher Scientific). The chromatographic separation was achieved by reverse-phase polar C18 (Kinetex Polar C18, 100 \times 2.1 mm, 2.6 μ m particle size, 100 Å pore size; Phenomenex, Torrance) with a SecurityGuard C18 column (2.1 mm ID) at 40°C column temperature. The mobile phase consisted of solvents A (water) and B (ACN) both containing 0.1% formic acid, and the flow rate was set at 0.5 mL/min. The gradient employed consisted of 0-1 min 1% B, 1-7.5 min 5-99% B, 7.5-9.3 min 99% B, 9.3-9.5 min 99-1% B, 9.5-11 min 1% B. Mass spectrometry (MS) analysis was performed using electrospray ionization (ESI) in positive ionization mode, and the parameters were set as follows: sheath gas flow 53 L/min, auxiliary gas flow rate 14 L/min, sweep gas flow 3 L/min, spray voltage 3.5 kV, inlet capillary to 269°C, and auxiliary gas heater 430°C. MS1 scan range was set to *m/z* 100-1,500

with a resolution ($R_{m/z\ 200}$) of 35,000, automatic gain control (AGC) target as 5.0E4, and maximum injection time of 100 ms. Up to 5 MS/MS spectra per MS1 were collected with a resolution ($R_{m/z\ 200}$) set to 17,500, AGC target as 5.0E5, and maximum injection time of 50 ms. The isolation window was set to 2 m/z and the isolation offset was set to 0 m/z . The normalized collision energy was acquired with an increased stepwise from 25 to 40 to 60%. The apex trigger was set to 1 to 5 s, the minimum AGC target for the MS/MS spectrum was 8.0E3, and a dynamic precursor exclusion of 10 s was selected. The data was deposited in GNPS/MassIVE and is publicly available at MSV000095648.

Immunomodulatory Activity assays

Co-culture of murine bone-marrow-derived dendritic cells (BMDCs) and naive CD4⁺ T cells with the pure synthetic *N*-acyl lipids was performed. In brief, BMDCs were generated from bone marrow progenitor cells isolated from femurs of wild-type C57BL6/J mice in the presence of 20 ng/mL GM-CSF (Miltenyi) in complete RPMI 1640 (10% FBS, 50 U mL⁻¹ penicillin, 50 µg/mL streptomycin, 2 mM L-glutamine, 1 mM sodium pyruvate, 1 mM HEPES, non-essential amino acids and β-mercaptoethanol). BMDCs co-cultured with splenic naive CD4⁺ T cells at a ratio of 1:10 (DC:CD4⁺ T cells) and treated with 50 µM of lipids in the presence of anti-mouse CD3 (2 µg/mL, eBiosciences), mouse IL-2 (20 µg/mL, Peprotech), mouse IL-6 (20 ng/mL, Peprotech) mouse IL-1b (20 ng/mL, Peprotech), mouse IL-23 (10 ng/mL, Life Technologies), and human TGFβ (2 ng/mL, Peprotech). After 3 days of co-culture, cells were stimulated with a cell activation cocktail with brefeldin A (2 µL/mL, BioLegend) for 5 h and stained for 30 min at 4 °C with Live/Dead fixable yellow dead stain kit (Life Technologies) at 1:1,000 dilution and with empirically titrated concentrations of the following antibodies: APC-eF780-conjugated anti-mouse CD4 (clone: RM4-5; eBioscience) at 1:400 dilution. For intracellular staining, cells were fixed and permeabilized using a Foxp3/Transcription Factor Staining buffer set (eBioscience) according to the manufacturer's protocol. Intracellular staining was performed using the following antibodies at the specified dilutions: FITC-conjugated anti-mouse Foxp3 (clone: FJK-16s; eBioscience) at 1:200 dilution; BV421-conjugated anti-mouse RORγt (clone: Q31-378; BD) at 1:100 dilution; and PE-Dazzle594-conjugated anti-mouse Tbet (clone: 4B10; BioLegend) at 1:200 dilution for 4 h at 4 °C. Cell acquisition was performed using a LSRFortessa X-20 (BD), and data were analyzed using FlowJo software suite (TreeStar). Data were visualized and analyzed using Prism v.10.4.1.

QUANTIFICATION AND STATISTICAL ANALYSIS

Retention time and MS/MS matching were performed between biological samples and combinatorial synthetic standard reaction mixtures. Extracts from skin samples of the body decomposition study (MSV000084322) and the HIV study (MSV000092833) were available in our laboratory for additional analyses to get retention time and MS/MS spectral matching between synthetic standards and biological samples. In addition, the samples from the microbial monocultures described in the "*Bacterial cultures screening*" section were used to confirm the microbial production of selected *N*-acyl lipids. Therefore, the biological samples and the synthetic standards were subjected to LC-MS/MS analyses. The dried extracts were resuspended in 150 µL of MeOH:H₂O (1:1, v/v) for the microbial extracts (n = 2) and the body decomposition samples (n = 4), while the HIV samples (n = 4) were resuspended in 150 µL of H₂O (100%). The same method described in "*Untargeted LC-MS/MS analysis of microbes from the multi-omics HIV analysis*" was used to acquire the data. However, two different gradients were used to evaluate the retention time matching between the synthetic *N*-acyl lipids and the compounds present in the biological samples: the first gradient (LC1) consisted of 0–1 min 1% B, 1–7.5 min 5–99% B, 7.5–9.3 min 99% B, 9.3–9.5 min 99–1% B, 9.5–11 min 1%B; and the second gradient (LC2) consisted of 0–1.5 min 1% B, 1.5–10.5 min 5–99% B, 10.5–12.3 min 99% B, 12.3–12.5 min 99–1% B, 12.5–14 min 1%B. The acquired LC-MS/MS data was deposited in GNPS/MassIVE and is publicly available at MSV000095423.

Source of the pure *N*-acyl lipids

Pure *N*-acyl lipids were acquired commercially from Sigma-Aldrich, Aldlab Chemicals, or EnamineStore. More specifically, *N*-(2-(1H-imidazol-4-yl)ethyl)acetamide (histamine-C2:0, purity 98%), *N*-(5-aminopentyl)acetamide (cadaverine-C2:0, purity 95%), *N*-(3,4-dihydroxyphenethyl)acetamide (dopamine-C2:0, purity 95%), and *N*-(2-(5-hydroxy-1H-indol-3-yl)ethyl)acetamide (serotonin-C2:0, purity >99%) were acquired from Sigma-Aldrich; *N*-(2-(1H-imidazol-4-yl)ethyl)propionamide (histamine-C3:0, purity 98%), *N*-(2-(1H-imidazol-4-yl)ethyl)butyramide (histamine-C4:0, purity 95%), *N*-(2-(1H-imidazol-4-yl)ethyl)pentanamide (histamine-C5:0, purity 98%), and *N*-(5-aminopentyl)propionamide (cadaverine-C3:0, purity 95%) were acquired from EnamineStore that synthesized them; and *N*-(2-(1H-imidazol-4-yl)ethyl)hexanamide (histamine-C6:0, purity 95%), *N*-(5-aminopentyl)pentanamide (cadaverine-C5:0, purity 95%), *N*-(5-aminopentyl)hexanamide (cadaverine-C6:0, purity 95%), *N*-(5-aminopentyl)heptanamide (cadaverine-C7:0, purity 95%), and propionyl-L-tryptophan (tryptophan-C3:0, purity 95%) were synthesized by Aldlab Chemicals.

The structure of these *N*-acyl lipids was confirmed by NMR ¹H. NMR spectra were collected at 298 K on a 600 MHz Bruker Avance III spectrometer fitted with a 1.7 mm triple resonance cryoprobe with z-axis gradients. The spectra were acquired in CD₃OD-*d*₄ or CDCl₃-*d*₁, which was chosen based on the solubility of the compounds. The shifts are reported in ppm and calibrated against the residual solvent signals at δ_H 3.31 and 7.26 for CD₃OD-*d*₄ and CDCl₃-*d*₁ respectively. The deuterated solvents were acquired from Cambridge Isotope Laboratories, Inc. (Andover, USA). The NMR data acquired were deposited in Zenodo (<https://doi.org/10.5281/zenodo.14015081>).

Quantification of *N*-acyl lipids in biological samples

The LC-MS/MS method used for the analyses of the method validation and quantification was the same as previously described in the beginning of this section, employing gradient LC1. The analytical method was performed according to the International Conference on Harmonization (ICH) guidelines¹²⁴ for histamine-C2:0, histamine-C3:0, histamine-C4:0, histamine-C5:0, cadaverine-C2:0, cadaverine-C3:0, cadaverine-C5:0, cadaverine-C6:0, and dopamine-C2:0. The method was validated based on the evaluation of the following parameters: specificity, precision (repeatability and intermediate precision), linearity, limit of detection (LOD), limit of quantification (LOQ), and accuracy. Detailed information regarding the methodology used for each of them is described below, and all the figures of merit are available in Table S3. The validation was performed using sample P3_D9_Sample_X3157299 from the HNRC cohort that would contain the compounds of interest. Skyline¹²⁵ (version 23.1) was used to extract the peak areas of the *N*-acyl lipids. The method employed reached the acceptance criteria specified for each parameter (Table S3). For quantification in biological samples, 148 samples of the HIV cohort were available and injected in the validated method (samples were resuspended in 100 μ L of H₂O containing 1 μ M of sulfamethazine). For the calculation of the amounts in the samples, it was estimated that 10 mg of stool sample would be the starting material, as previously described,¹²⁶ and the extraction yield was also extrapolated to 100%. In addition, all the samples of the microbial monocultures described in the "Microbial cultures from the multi-omics analysis" were also analyzed. The injection volume was set to 2 μ L for all samples.

Specificity

The specificity was determined by injecting a blank solution containing only the internal standard (sulfadimethazine), and an injection of a solution containing all the *N*-acyl lipids ($n=3$). The relative standard deviation (RSD) was calculated based on each peak's retention time in the P3_D9_Sample_X3157299 sample. The MS and MS/MS spectra confirmed the specificity and identity of these compounds. The retention times of the peaks of interest were as follows: histamine-C2:0, 0.58 min; histamine-C3:0, 0.73 min; histamine-C4:0, 1.13 min; histamine-C5:0, 2.29 min; cadaverine-C2:0, 0.61 min; cadaverine-C3:0, 0.78 min; cadaverine-C5:0, 2.47 min; cadaverine-C6:0, 2.94 min; dopamine-C2:0, 2.60 min. These compounds didn't show interferences compared to the solution containing only the mixture of standards.

Precision (repeatability and intermediate precision)

The precision of the method was determined by analyzing the P3_D9_Sample_X3157299 sample in six replicates ($n=6$), and the repeatability (intra-day precision) was estimated as the RSD of the standards concentrations (μ g/mL) measured in two consecutive days. The concentrations calculated for the compounds on both days are available in Table S3. The RSD values were lower than 5%, and the F-test between the two days showed no significant difference at $F=0.05$.

Linearity

The linearity of the method was determined by calibration curves in concentration ranges comprising each compound at the samples of interest. A stock solution containing 60 μ g/mL of each *N*-acyl lipid was prepared in H₂O (100%) and used to acquire calibration curves for all the compounds simultaneously. From this solution, 6 to 13 points were prepared with levels ranging from 0.001 to 20 μ g/mL, and each concentration level was injected in triplicate. The analytical curves were built based on the nominal concentrations, and the average between the ratios of each compound and the internal standard used ($\text{Ratio} = A_{\text{compound}}/A_{\text{IS}}$). A polynomial equation was obtained for each curve, and the correlation coefficients (R) were calculated for each compound. The linear ranges and R coefficients are available in Table S3.

Limit of detection and limit of quantification

LODs and LOQs were estimated by the mean of the slopes (a) and the standard deviation of the y-intercept (S_b) on three calibration curves (linear regression was used) in three low concentrations for each compound (0.002 to 0.02 μ g/mL). A linear regression was used in this estimation. These limits were calculated by the following equations: $\text{LOD} = (3.3 \cdot S_b)/a$ and $\text{LOQ} = (10 \cdot S_b)/a$. All the slopes, intercepts, LODs, and LOQs are shown in Table S3.

Accuracy

The accuracy of the method was determined by recovery analyses. For this, known amounts of the solution containing the standards were spiked to the P3_E10_Sample_x3137731 and P3_G2_Sample_X3148765 sample solutions in two different concentrations (low and high) considering the predetermined calibration curve and concentration range. Three replicates for each level were injected and analyzed in the validated method. The accuracy was determined by the difference between the theoretical and experimental concentration values and the values were within the acceptance range of 80–120%.

Statistical analyses

Statistical tests for the re-investigation of public metabolomics datasets were performed using the non-parametric Mann-Whitney U test in cases where two groups were being compared (diabetes, diet, antibiotic treatment, HIV status, neurocognitive impairment—Figures 2E, 2F, S3H, S3M, S3N, and S5A–S5C), or with the non-parametric Kruskal-Wallis for more than two groups (body decomposition—Figures S3, S3K, and S3L). The p -values were corrected for multiple comparisons using the Benjamini-Hochberg correction. The statistical tests were done with the "scipy.stats" package (version 1.7.3), and the p -values corrections with the "statsmodels.stats.multitest" (version 0.11.1) in Python (version 3.7.6).

For the HNRC study, the differences in individual *N*-acyl lipids between the study groups were compared using a multivariate linear mixed-effects model with fixed covariates for HIV status (PWH vs. PWOH) and neurocognitive impairment status (impaired vs. unimpaired) (\sim HIV status + neurocognitive impairment), while accounting for random effects within individual samples (~ 1 | Subject) using

the MaAsLin2 package in R (version 4.2.1). Lipid values were log-transformed, and zero values were imputed with half the minimum value prior to analysis. The regression coefficients from the linear model were illustrated as a forest plot using the 'ggplot2' (version 3.5.1) package in R (version 4.2.1). This analysis was also repeated considering only the PWH subgroup with fixed covariates for neurocognitive impairment status. To visualize the correlation coefficients from the linear model with only fixed effects (i.e., the association between CD4/CD8 ratio or plasma viral load considering only the PWH subgroup), a horizontal bar plot was created using 'ggplot2' (version 3.5.1). The color palettes were selected from the RColorBrewer (version 1.1.3) package in R (version 4.2.1).

Statistical tests for the immunomodulatory assays results were conducted in R (v.4.3.3) by using the "stats" package to run a one way ANOVA test and the "multcomp" package to perform Dunnett's multiple comparisons analysis. Significance was considered for $p < 0.05$ between the control (DMSO) and treated cells.

Supplemental figures

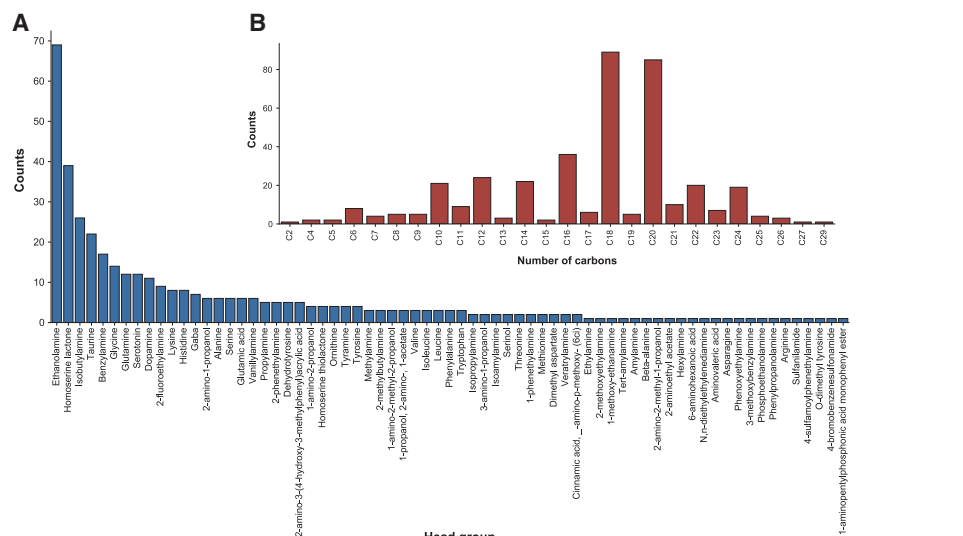


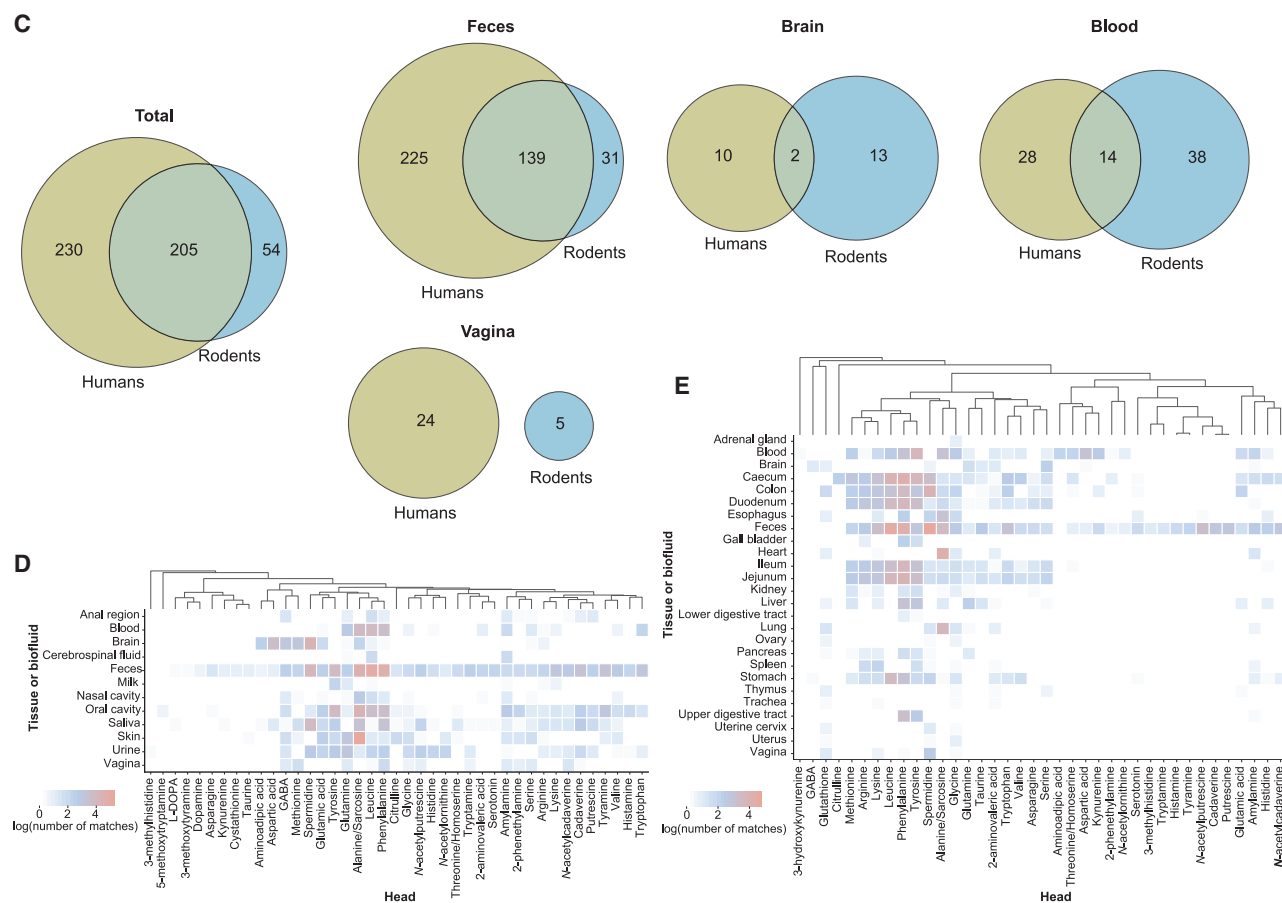
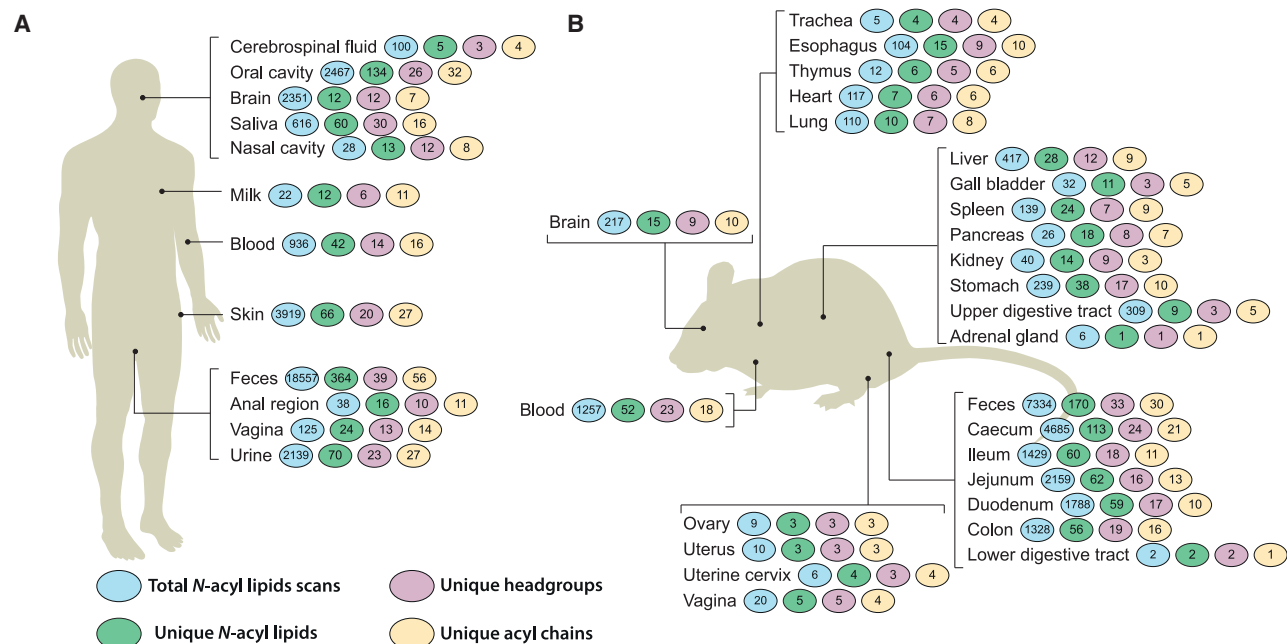
Figure S1. Distribution of *N*-acyl lipids in structural databases and mass spectrometry repository searches, related to Figure 1

(A) Diversity and relative frequency of *N*-acyl lipids head groups and (B) lipid chain lengths documented in LIPID MAPS. This analysis excludes ceramide acylations.

(C) *N*-Acyl lipid query strategy: representative MS/MS spectra of phenylalanine-C10:0 (CCMSLIB00011435104) and phenylalanine-C16:0 (CCMSLIB00011435452). The spectra show nearly identical fragmentation patterns, enabling the creation of the MassQL query to retrieve the MS/MS spectra of this family of lipids.

(D) MassQL query for phenylalanine head group where we initiate to return all MS/MS spectra (in yellow) that fulfill the following criteria: the precursor ion has to match one of the expected precursor *m/z* values specified (gray), as well as the most diagnostic *m/z* fragments of the head portion (blue and pink) with their indicated error tolerances and minimum relative intensities.

(E) Strategy followed to create the *N*-acyl lipid library and expand to biological interpretations. (I) MassQL queries were designed and run against the Orbitrap datasets in the GNPS/MassIVE repository. (II) The spectra were clustered using MSCluster to reduce redundancy. (III) A cosine similarity filter was applied to keep the higher-confidence *N*-acyl lipids spectra. (IV) The clustered spectra were searched using FASST searches against the whole repository (including Orbitrap and QToF datasets), and human and rodent-related datasets were tagged using ReDU, and microbial, plant, and food-related datasets were also tagged using domain-specific MASSTs. (V) The spectra retrieved from the FASST searches were filtered to keep the matches in which the raw (unfiltered) spectra resulted in cosine similarity above 0.7. (VI) Summary of the results obtained with this workflow. Icons were obtained from [Bioicons.com](https://www.bioicons.com).



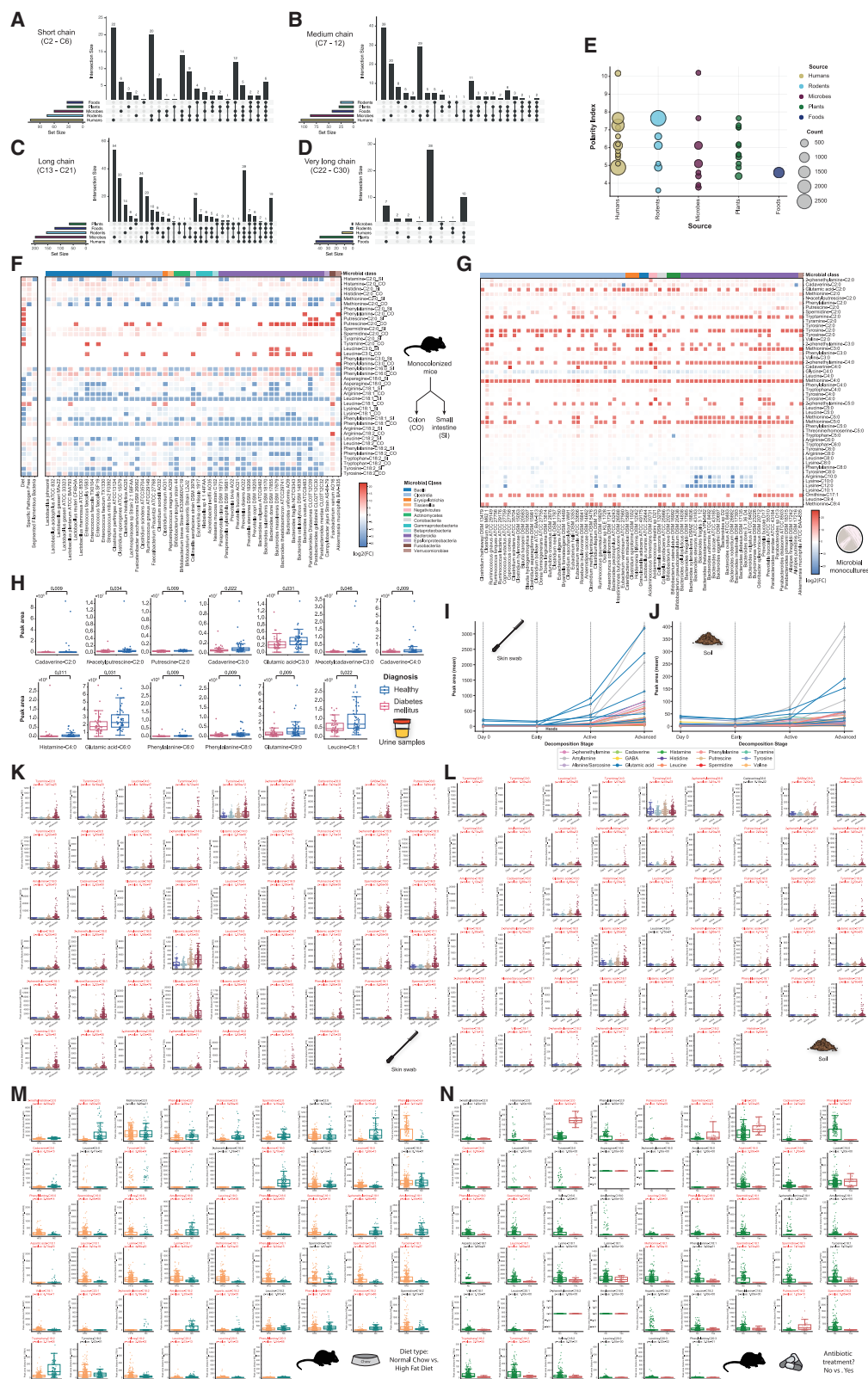
(legend on next page)

Figure S2. Distribution of *N*-acyl lipids obtained from FASST searches among different tissues or biofluids, related to Figure 1

(A and B) Summary of the occurrences in the public domain in (A) human- and (B) rodent-related datasets.

(C) Venn diagrams illustrate the distribution of unique *N*-acyl lipids in human- and rodent-related datasets. The data are further stratified by tissues and biofluids shared between the organisms.

(D and E) Heatmaps show the distribution of the number of matches grouped by head group in different tissues and biofluids with metadata available in ReDU for (D) human- and (E) rodent-related public datasets. All heatmaps are shown as log values of the matches obtained from the repository. Icons were obtained from [Bioicons.com](https://bioicons.com).



(legend on next page)

Figure S3. *N*-Acyl lipids' chain length diversity, evidence of microbial *N*-acyl lipids, and reanalysis of public datasets, related to Figure 2

(A–D) Distribution of *N*-acyl lipids in public data stratified by chain length classes. Upset plots show the number of unique *N*-acyl lipids attached to (A) short-, (B) medium-, (C) long-, and (D) very long-chain fatty acids.

(E) Estimated polarity indexes of solvent mixtures used as extraction solvents in the datasets retrieved in the repository-scale analyses. Snyder's indexes were used to calculate them through a weighted equation.

(F) Reanalysis of a public dataset of monocolonized germ-free (GF) mice (GNPS/MassIVE: MSV000088040, deposited in 2021).^{32,33} Heatmap log₂ fold changes (FCs) of the *N*-acyl lipids matches in colon and small intestine samples of monocolonized mice relative to GF mice. Values of the diet, specific pathogen-free (SPF) mice, and of mice colonized with segmented filamentous bacteria (SFB) are also shown. Red cells indicate compounds that are increasing relative to GF, while blue cells indicate compounds that are decreasing relative to GF mice. The x axis is taxonomically ordered according to the NCBI Taxonomy ID.

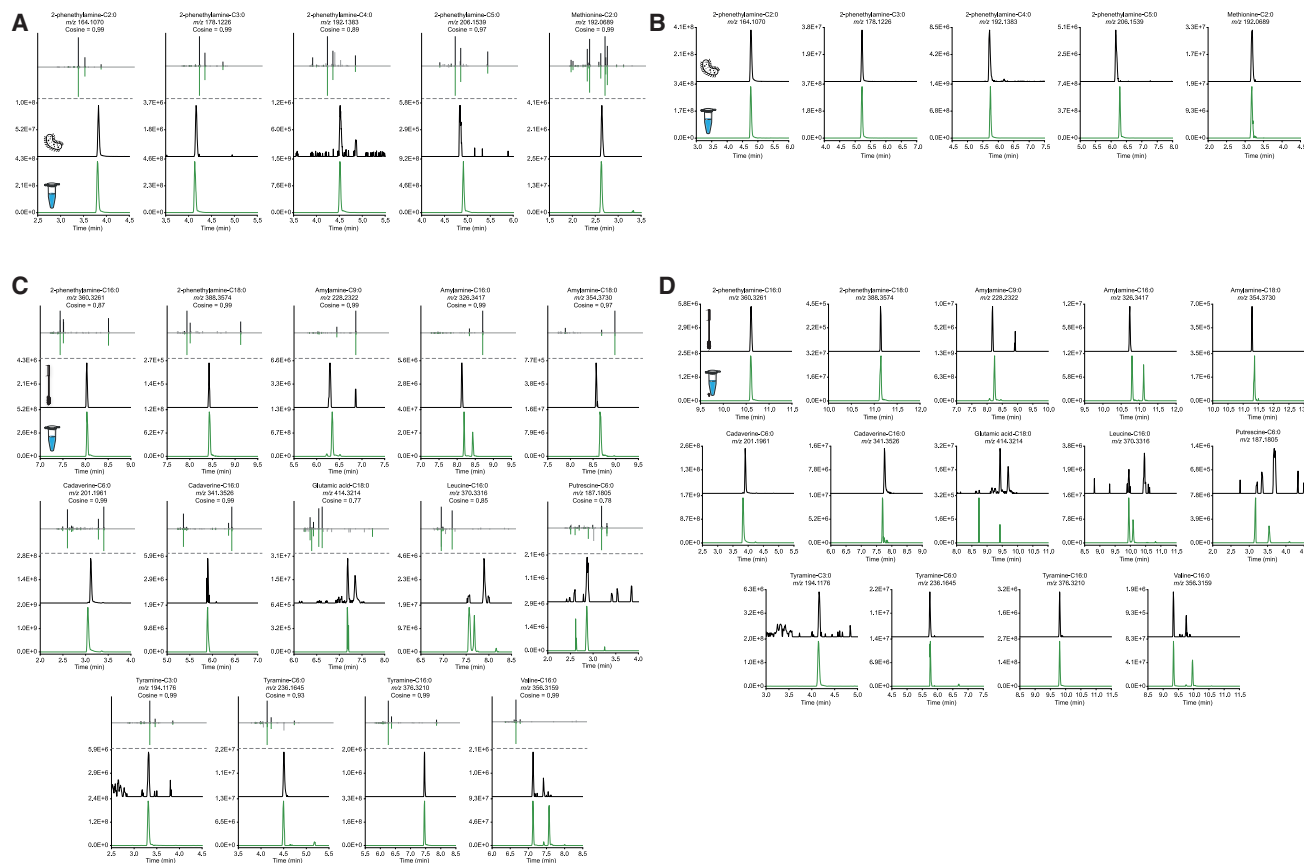
(G) Heatmap showing the log₂ FC of *N*-acyl lipid matches in microbial monocultures of gut commensal microbes relative to the culture media. Red cells indicate compounds that are increasing, while blue cells indicate compounds that are decreasing relative to the media. The x axis is taxonomically ordered according to the NCBI Taxonomy ID.

(H) Peak area abundances of *N*-acyl lipids annotated in a public dataset (GNPS/MassIVE: MSV000082261) from urine samples across clinical groups of healthy and type I diabetes mellitus. Only *N*-acyl lipids with *p* values of 0.05 or less are shown. Healthy, *n* = 52; diabetes (type 1), *n* = 44.

(I and J) *N*-Acyl lipids annotated from a public dataset (GNPS/MassIVE: MSV000084322, MSV000084463) of (I) skin swabs and (J) soil samples of a human cadaver decomposition study.³⁶ The parallel coordinate plots show the mean of the *N*-acyl lipid peak areas obtained for the different head groups in each stage of decomposition. Each line represents a *N*-acyl lipid match.

(K and L) Peak area abundances of *N*-acyl lipids annotated in public datasets from (K) skin (GNPS/MassIVE: MSV000084322) and (L) soil (GNPS/MassIVE: MSV000084463) samples across different stages of decomposition of human bodies.³⁶ Skin: day 0, *n* = 36; early, *n* = 171; active, *n* = 292; advanced, *n* = 249. Soil: day 0, *n* = 36; early, *n* = 171; active, *n* = 299; advanced, *n* = 252.

(M and N) Peak area abundances of *N*-acyl lipids annotated in a public dataset (GNPS/MassIVE: MSV000080918)³¹ from mice fecal samples of mice subjected to different diets (M) and treatment with a cocktail of antibiotics (N). Antibiotics: no, *n* = 310; yes, *n* = 27. Diet: high-fat diet (HFD), *n* = 310; normal chow (NC), *n* = 114. For the antibiotics plot, only mice fed with HFD were considered. All boxplots indicate the first (lower), median, and third (upper) quartiles, while whiskers are 1.5 times the interquartile range. Significance was tested in cases where two groups were compared using the non-parametric two-sided Mann-Whitney U test, while for more than two groups, the non-parametric Kruskal-Wallis test was used, and *p* values were corrected for multiple comparisons using the Benjamini-Hochberg correction. Compounds with *p* values below 0.05 are highlighted in red. Icons were obtained from [Bioicons.com](https://bioicons.com).



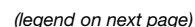


Figure S5. *N*-Acyl lipids associated with HIV status, HIV plasma viral load, and neurocognitive impairment status, related to Figure 3

- (A) Peak area abundances of *N*-acyl histamines in people with HIV (PWH) and people without HIV (PWoH) (PWH, $n = 228$; PWoH, $n = 93$).
- (B) Peak area abundances of *N*-acyl polyamines in cognitively impaired and normal participants (impaired, $n = 151$; unimpaired, $n = 162$) of the HNRC.
- (C–E) Peak area abundances of *N*-acyl polyamines in cognitively impaired and normal participants (impaired, $n = 114$; unimpaired, $n = 112$) within the PWH subgroup. Boxplots indicate the first (lower), median, and third (upper) quartiles, while whiskers are 1.5 times the interquartile range. Significance was tested using the non-parametric two-sided Mann-Whitney U test. The p values shown are nominal p values, and the adjusted ones (for multiple comparisons using Benjamini-Hochberg) are also available in Table S3. Molecular networks obtained for the (D) *N*-acyl histamines and (E) *N*-acyl cadaverines. The molecular networks were created using the feature-based molecular networking workflow⁹⁷ within the GNPS environment.²² The nodes are annotated based on spectral similarity matches with the *N*-acyl lipids library created. The nodes represent each MS/MS spectrum, while the edges connecting them represent their spectral similarity (threshold set to cosine > 0.7). Pie charts indicate the relative abundance of ion features in each group highlighted. This dataset is publicly available in GNPS/MassIVE under the accession number MSV000092833.
- (F) Forest plot illustrating the coefficient estimate of a linear mixed-effects model for individual *N*-acyl lipids, with fixed covariates of neurocognitive impairment status (PWH subset; impaired, $n = 114$; unimpaired, $n = 112$), accounting for random effects within individual samples/visit where stool samples were collected. Filled circles with corresponding confidence intervals represent significant *N*-acyl lipid species. Faded circles and squares depict non-significant species. Each color represents a different head group.
- (G) Bar plots showing the correlation coefficients for the association between HIV RNA viral load and various *N*-acyl lipids in the PWH ($n = 203$). Red bars represent positive correlations, while blue bars represent negative correlations, as determined by linear regression models. The p values shown are nominal; adjusted p values (corrected for multiple comparisons using the Benjamini-Hochberg method) are available in Table S3.
- (H) MS/MS mirror plots and retention time matches to the pure *N*-acyl lipids standards. MS/MS spectra on the top (black) represent the ones detected in the HNRC fecal samples, while the MS/MS on the bottom (green) are the ones obtained from the standards. Chromatographic traces represent the exported ion chromatograms for each compound (black: sample; green: standard). The chromatographic method LC1 (see STAR Methods) was used. MS/MS mirror plots can be interactively inspected in the metabolomics spectrum resolver,¹²⁷ with the information provided in Table S3.
- (I) Chromatographic traces represent the exported ion chromatograms for each compound (black: sample; green: standard), with data acquired in a different chromatographic method: LC2 (see STAR Methods).
- (J) Microbe-metabolite co-occurrence biplot obtained from mmvec⁴¹ analysis of the HNRC sample. Spheres represent ions of molecules, while arrows represent microbes. Spheres were colored based on in which group (PWH vs. PWoH) each ion feature was most abundant. Small angles between the arrows indicate microbes co-occurring with one another, and spheres close in the plot represent features co-occurring. Arrows pointing toward a group of molecules indicate microbe-molecule co-occurrence. This biplot shows the 30 most important OTUs (higher vector magnitude). The biplot can be interactively visualized using EMPeror,¹²³ with the QZV file provided at <https://doi.org/10.5281/zenodo.14015198>.